A Sub-7-GHz Linear Receiver for 5G Local Area Base Station Applications

Montazerolghaem, Mohammad Ali; Babaie, Masoud

DOI
10.1109/JSSC.2025.3551673

Publication date
2025

Document Version
Final published version

Published in
IEEE Journal of Solid-State Circuits

A Sub-7-GHz Linear Receiver for 5G Local Area Base Station Applications

Mohammad Ali Montazerolghaem, *Member, IEEE*, and Masoud Babaie, *Senior Member, IEEE*

***Abstract*— This article presents a sub-7-GHz receiver (RX) for the fifth-generation (5G) local area base station applications. A Rauch transimpedance amplifier (TIA) with a third-order high-pass impedance in its feedback is adopted to enhance RX selectivity and provide higher loop gain (LG) at the bandwidth edge, improving in-band linearity for high-bandwidth applications. An N-path notch filter, sharing switches with down-converting passive mixers, is incorporated in the low-noise transconductance amplifier (LNTA) to enhance out-of-band linearity without limiting the RX's operating frequency. Additionally, a frequency-dependent negative capacitance is realized at the LNTA input by exploiting the bandpass characteristic of the TIA input impedance, which helps achieve a flat in-band response, extend the RX bandwidth, and improve front-end filtering roll-off. Fabricated in 40-nm CMOS technology, the RX occupies a 1.3-mm^2 area, operates from 0.4 to 7.3 GHz, and consumes 105–195 mW from a 1.3-V supply. It achieves a third-order output third-order intercept point (OIP3) of 27–38 dBm over a 300-MHz channel bandwidth and a noise figure (NF) of 3.2–5.8 dB across its operating range. With its high linearity, low NF, and enhanced selectivity, the RX satisfies 3GPP standard requirements for reference sensitivity, in-band blocking, close-in blocking, and far-out blocking.**

***Index Terms*— Current-mode receivers, fifth-generation (5G) local area base station applications, high-bandwidth applications, high loop gain (LG), in-band linearity, positive feedback, Rauch transimpedance amplifier (TIA), selectivity.**

I. Introduction

LOW-BAND and mid-band frequencies in new radio (NR) systems are expected to remain the backbone of the fifth generation (5G) of mobile communication due to their low path loss, which enhances network coverage. However, to address the relentless customer demand for higher data rates, the operating frequency and RF bandwidth (BW_{RF}) of 5G local area base station receivers (RXs) have been extended to 7.125 GHz and 400 MHz, respectively [1]. Typically, modern RXs use current-mode architectures to achieve a high operating frequency and BW_{RF}. Current-mode RXs avoid any RF voltage gain before baseband filtering to enhance their linearity performance. Despite their advantages, current-mode RXs still face the following challenges in meeting the stringent requirements of 5G applications.

The operating frequency of wideband RXs is often constrained by parasitic capacitors at the RF nodes. For instance, in mixer-first RXs, large passive mixers are typically required to achieve a fair noise figure (NF), which introduces significant parasitic capacitance and limits the operating frequency of most prior art mixer-first RXs to below 5 GHz [2], [3], [4], [5], [6], [7], [8], [9], [10], [11], [12], [13], [14], [15], [16], [17]. Similarly, in low-noise transconductance amplifier (LNTA)-based RXs, an N-path notch filter is commonly used in the LNTA's feedback to improve out-of-band linearity, but this also adds parasitic capacitance at the LNTA's output, restricting their operating frequency to below 6 GHz [18], [19], [20], [21], [22], [23], [24], [25], [26], [27], [28], [29], [30], [31], [32], [33]. Therefore, additional techniques are required to achieve higher operating frequencies without sacrificing RX linearity or NF performance.

Moreover, as shown in Appendix A, the RX's output third-order intercept point (OIP3) must be at least 22.5 dBm to handle a −35-dBm modulated in-band blocker. Since the in-band signals are not filtered, the in-band linearity is mainly limited by the transimpedance amplifier (TIA) [34], [35], [36]. To ensure sufficient loop gain (LG) to meet the in-band linearity requirements, the TIA amplifier must provide a high dc gain (A_0), ideally greater than 60 dB, as suggested in [36]. Additionally, to prevent impedance peaking in the TIA input impedance, the TIA amplifier's dominant pole must be at least half of the desired baseband bandwidth (i.e., $BW_{RF}/2$), which can reach up to 200 MHz. This necessitates a TIA unity gain bandwidth (ω_u) exceeding 200 GHz, a challenging and power-hungry number. In practice, however, ω_u is much smaller, causing input impedance peaking at the bandwidth edge and degrading in-band linearity [37]. Therefore, a TIA structure with lower sensitivity to ω_u is highly desirable for maintaining linearity in wideband 5G RXs.

Despite the wider RF bandwidth required for 5G applications, the offset frequency of close-in blockers from the passband edges remains constant. For example, the offset frequency of a −15-dBm close-in blocker is only 60 MHz for mid-band radios operating above 3 GHz [1]. To effectively handle this blocker, the TIA must meet two critical requirements. First, the TIA's filtering must sufficiently suppress close-in blockers to prevent voltage clipping at the TIA's output. Second, the LG of the TIA amplifier must be adequately high, not only within the 3-dB bandwidth to handle the in-band blocker but also at the bandwidth edge to suppress intermodulation between the in-band and close-in blockers.

Received 19 November 2024; revised 10 February 2025 and 7 March 2025; accepted 7 March 2025. Date of publication 27 March 2025; date of current version 29 October 2025. This article was approved by Associate Editor Yunzhi Dong. This work was supported by the Nederlandse Organisatie voor Wetenschappelijk Onderzoek (NWO)/Ampleon Partnership Program under Project 16336. *(Corresponding author: Mohammad Ali Montazerolghaem.)*

The authors are with the Department of Microelectronics, Delft University of Technology, 2628 CD Delft, The Netherlands (e-mail: m.a.montazerolghaem-1@tudelft.nl).

Color versions of one or more figures in this article are available at https://doi.org/10.1109/JSSC.2025.3551673.

Digital Object Identifier 10.1109/JSSC.2025.3551673

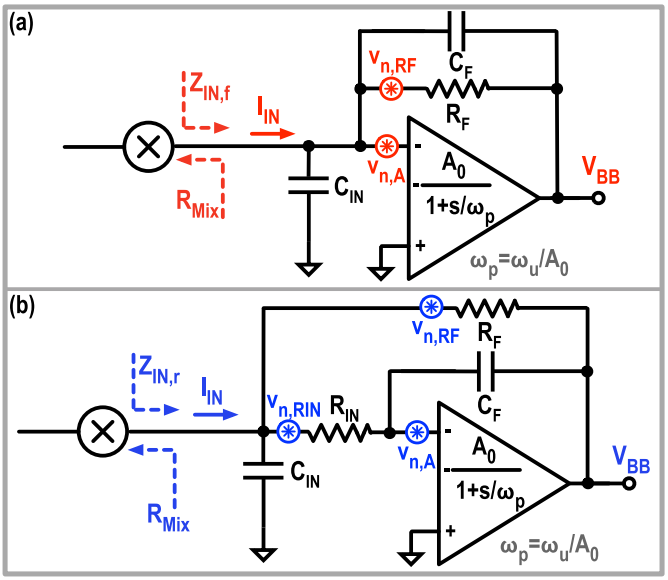

Fig. 1. Block diagram of (a) first-order TIA and (b) Rauch TIA.

These conditions impose stringent demands on the TIA design.

Finally, in local area co-location applications, the RX must be capable of handling a −4-dBm far-out out-of-band blocker in local area co-location applications. Since the frequency of the co-location blockers remains fixed, the RX's out-of-band rejection at the blocker's offset frequency is constrained by the increased channel bandwidth of 5G applications and the order of the RF front-end filtering. Therefore, a new RF front-end scheme is needed to extend the 3-dB bandwidth while maintaining the out-of-band rejection and the operating frequency range.

As an extension of [38], this article introduces an LNTA-based RX to address the challenges outlined earlier. First, it employs a Rauch TIA to achieve a second-order response and higher LG near the bandwidth edge, two key features required in high-bandwidth applications. A third-order impedance is incorporated in the TIA feedback network to further improve the RX's selectivity and suppress close-in blockers. Moreover, one set of N-path notch filter switches is merged with the down-converting switches to minimize the parasitic capacitance at the LNTA output and enhance the RX operating frequency. Finally, leveraging the input impedance of Rauch TIA, a positive feedback technique is introduced to boost $\mathrm{BW_{RF}}$ while maintaining the out-of-band linearity.

The article is organized as follows. Section II provides an in-depth analysis of the Rauch TIA, comparing it to the first-order TIA to demonstrate its advantages for 5G applications. Sections III and IV present the RF front-end architecture and analyze the RX in-band linearity, respectively. Section V covers the RX circuit implementation, followed by experimental results in Section VI. Finally, Section VII concludes this article.

II. Transimpedance Amplifier

As mentioned earlier, the TIA limits the in-band linearity performance of current-mode RXs. Therefore, we compare two well-known TIA structures in this section to identify the better candidate for 5G applications. Fig. 1 shows the block diagrams of the first-order and Rauch TIAs [39]. Both TIAs use feedback impedance, comprising R_F and C_F, to convert the input current to a baseband voltage, with C_{IN} placed at the TIA input to absorb the out-of-band blocker current. Unlike the first-order TIA, the Rauch TIA includes an extra series resistor, R_{IN}, between the TIA input and its amplifier input. The values of R_F and C_{IN} are chosen based on the gain and out-of-band blocker current requirements and are kept the same for both structures to ensure similar area, gain, and power consumption. We then compare the two structures in terms of transfer function, input impedance, linearity, performance under process, voltage, and temperature (PVT) variations, noise, and dc offset with C_F adjusted to achieve the same 3-dB bandwidth ($\omega_{3\,\mathrm{dB}}$) for both structures.

A. Transfer Function

First, the transfer functions of both TIAs are calculated and compared. The frequency response of the first-order TIA can be calculated as follows:

$$Z_{21,f} = \frac{V_{\mathrm{BB}}}{I_{\mathrm{IN}}} = -\frac{R_F}{sR_F\left(C_F + \frac{C_F}{A(s)} + \frac{C_{\mathrm{IN}}}{A(s)}\right) + 1} \tag{1}$$

where V_{BB} and I_{IN} are the TIA's output voltage and input current, respectively. Furthermore, $A(s)$ is the gain of the TIA amplifier and is given by

$$A(s) = \frac{A_0}{1 + \frac{s}{\omega_p}} \tag{2}$$

where ω_p is the dominant pole of the TIA amplifier. Assuming that $A(s)$ is large enough across the 3-dB bandwidth, the transfer function is a first-order response and $R_F C_F$ sets the 3-dB bandwidth. On the other hand, the transfer function of the Rauch TIA can be calculated as follows:

$$Z_{21,r} = -\frac{R_F}{s^2 R_{\mathrm{IN}} C_{\mathrm{IN}} R_F C_F + s(R_{\mathrm{IN}} + R_F)C_F + 1} \tag{3}$$

which shows a second-order low-pass response. Assuming that $R_F \gg R_{\mathrm{IN}}$, the natural frequency (ω_n) and damping ratio (ζ) can be calculated as

$$\zeta = \frac{1}{2}\sqrt{\frac{R_F C_F}{R_{\mathrm{IN}} C_{\mathrm{IN}}}} \tag{4}$$

$$\omega_n = \sqrt{\frac{1}{R_{\mathrm{IN}} C_{\mathrm{IN}} R_F C_F}}. \tag{5}$$

Moreover, the 3-dB bandwidth of the Rauch TIA is given by

$$\omega_{3\,\mathrm{dB}} = \omega_n\sqrt{1 - 2\zeta^2 + \sqrt{\left(2\zeta^2 - 1\right)^2 + 1}}. \tag{6}$$

Fig. 2(a) compares the transfer function of the first-order and Rauch TIAs with nearly identical components, except for R_{IN} to achieve the same gain and 3-dB baseband bandwidth. Thanks to the complex conjugate poles of the Rauch TIA, it exhibits a flat in-band gain and a second-order low-pass response, which is desirable for 5G applications.

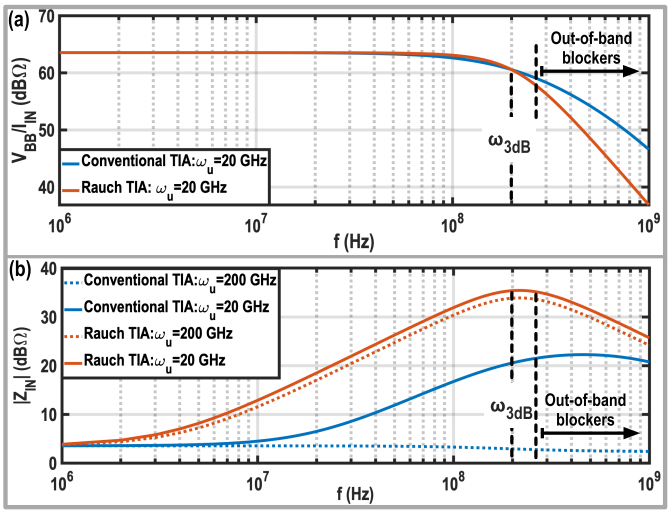

Fig. 2. Simulated (a) transfer function and (b) input impedance of the first-order TIA and Rauch TIA in MATLAB (first-order TIA: $C_{IN} = 10$ pF, $R_F = 1.5$ kΩ, $C_F = 605$ fF, and $A_0 = 60$ dB; Rauch TIA: $C_{IN} = 10$ pF, $R_{IN} = 50$ Ω, $R_F = 1.5$ kΩ, $C_F = 720$ fF, and $A_0 = 60$ dB) for different unity gain bandwidths.

B. Input Impedance

Second, the input impedance (Z_{IN}) of both structures is compared. Considering that $A(s) \gg 1$, the input impedance of the first-order TIA is derived as follows:

$$Z_{IN,f} = \frac{R_F}{A(s)} \cdot \frac{1}{sR_F\left(C_F + \frac{C_{IN}}{A(s)}\right) + 1} \tag{7}$$

$$\xrightarrow{C_F \gg \frac{C_{IN}}{A(s)}} Z_{IN,f} \approx \frac{R_F}{A_0} \cdot \frac{1 + \frac{s}{\omega_p}}{1 + sR_FC_F}. \tag{8}$$

Hence, the input impedance of the first-order TIA consists of one zero, determined by the TIA amplifier's dominant pole, and one pole at $1/R_FC_F$. Typically, $1/R_FC_F$ also defines the TIA's 3-dB bandwidth, $\omega_{3\,dB}$. Consequently, as can be gathered from (8), setting $\omega_p \geq \omega_{3\,dB}$ ensures that the TIA input impedance remains approximately constant across the in-band frequencies.

As shown in Fig. 2(b), in a desired scenario ($\omega_p \geq \omega_{3\,dB}$), $Z_{IN,f}$ remains low and constant (i.e., R_F/A_0) across the 3-dB bandwidth. However, as discussed earlier, to meet this condition with $A_0 \geq 60$ dB, the unity gain bandwidth of the TIA amplifier must exceed 200 GHz ($\omega_u = A_0 \cdot \omega_p$), which, if not impossible, is a highly challenging and power-hungry requirement. A more realistic value for ω_u is around 20 GHz, resulting in ($\omega_p \ll \omega_{3\,dB}$). Hence, $Z_{IN,f}$ remains R_F/A_0 near dc but begins to increase at ω_p, reaching its maximum at the bandwidth edge. Beyond $\omega_{3\,dB}$, the input impedance becomes nearly constant due to the pole created by R_F and C_F. At higher baseband frequencies, C_{IN} dominates, reducing $Z_{IN,f}$. Therefore, the input impedance of the first-order TIA is highly sensitive to the TIA amplifier's gain bandwidth and PVT variations.

The input impedance of Rauch TIA can be calculated by

$$Z_{IN,r} = \frac{R_F}{A(s)} \cdot \frac{sA(s)C_FR_{IN} + 1}{s^2R_{IN}C_{IN}R_FC_F + s(R_{IN} + R_F)C_F + 1}. \tag{9}$$

Due to its low-frequency zero at $1/(A_0C_FR_{IN})$, even when ($\omega_p \geq \omega_{3\,dB}$), $Z_{IN,r}$ increases from R_F/A_0 near dc to $R_{IN} \| R_F \approx R_{IN}$ at the bandwidth edge. It then drops by −20-dB/dec slope due to the complex poles at $\omega_{3\,dB}$. This bandpass behavior will later be leveraged to improve the selectivity and bandwidth of the RF front end. Interestingly, as can be gathered from Fig. 2(b), $Z_{IN,r}$ is primarily determined by the passive components and is largely insensitive to the amplifier gain and ω_u. However, since $Z_{IN,r}$ at the bandwidth edge approaches R_{IN}, the input impedance of the Rauch TIA can exceed that of the first-order TIA. Consequently, in LNTA-based RXs, designers must consider potential in-band linearity degradation due to the increased load on the LNTA. The impact of Rauch TIA impedance peaking on RX in-band linearity will be discussed later in this article.

C. Linearity

Next, the linearity of both TIA structures is evaluated by comparing their input/output voltage swing and the LG. As shown in Fig. 2(a), the in-band transfer functions of both TIAs are nearly identical. The output voltage swing of the TIA amplifier is $-R_FI_{IN}$ for both, resulting in a corresponding input voltage of $R_FI_{IN}/A(s)$. Therefore, the input and output voltage swings of the TIA amplifiers are the same for in-band input signals.

Another key factor influencing the TIA's in-band linearity is LG. The LG of the first-order TIA is calculated as follows:

$$\text{LG} = \frac{-R_{Mix}}{R_{Mix} + R_F} \cdot \frac{A_0}{1 + \frac{s}{\omega_p}} \cdot \frac{sR_FC_F + 1}{sR_F \| R_{Mix}C_{IN} + 1} \tag{10}$$

where R_{Mix} is the impedance seen from the baseband port of passive mixers toward the RF front end. The LG has two poles (ω_p and $1/(R_F \| R_{Mix}C_{IN})$) and one zero ($1/(R_FC_F)$). As discussed earlier, in most practical cases, ω_p lies within the 3-dB bandwidth, acting as the dominant pole and decreasing the LG with a −20-dB/dec slope. Unfortunately, the second pole, $1/(R_F \| R_{Mix}C_{IN})$, typically lies below $\omega_{3\,dB}$ since C_{IN} is much larger than C_F to absorb far-out out-of-band blocker current. Consequently, the LG experiences −40-dB/dec roll-off at the passband edge due to the second pole. Eventually, the zero at the bandwidth edge increases the slope back to −20 dB/dec, improving TIA's stability [40]. As can be gathered from Fig. 3, TIA in-band linearity is expected to worsen at the passband edges due to the significant drop in LG. Reducing C_{IN} shifts the second pole to higher frequencies, thus increasing the LG at the passband edges. However, C_{IN} also absorbs the out-of-band blocker currents. Hence, reducing C_{IN} increases the blocker swing at the baseband port of passive mixers, which degrades the out-of-band linearity performance of LNTA and passive mixers. This issue creates a tradeoff between in-band and out-of-band linearity.

The LG of the Rauch TIA is derived as

$$\text{LG} \approx \frac{-R_{Mix}}{R_{Mix} + R_F} \cdot \frac{A_0}{1 + \frac{s}{\omega_p}} \cdot \frac{s^2R_{IN}C_{IN}R_FC_F + s(R_{IN} + R_F)C_F + 1}{(sR_F \| R_{Mix}C_{IN} + 1)(sR_{IN}C_F + 1)}. \tag{11}$$

The LG of Rauch TIA has three poles and two zeros. The first two poles ω_p and $1/(R_F \| R_{Mix}C_{IN})$ are the same as those in the

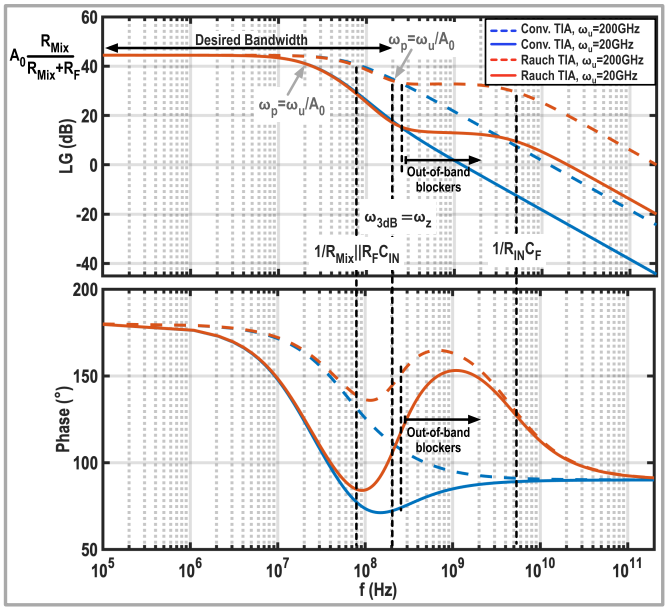

Fig. 3. Bode plot of simulated LG for the first-order and Rauch TIAs.

first-order TIA, while the third pole, $1/(R_{\rm IN}C_F)$, is located far from the bandwidth edge. Consequently, the in-band response of the Rauch TIA's LG is similar to that of the first-order TIA. However, as illustrated in Fig. 3, the Rauch TIA LG also has two zeros at the bandwidth edge, which flattens the LG at the close-in out-of-band frequencies. This higher LG at out-of-band frequencies helps suppress intermodulation between in-band and close-in blockers, which can fall within the 3-dB bandwidth and degrade RX performance. Consequently, the Rauch structure exhibits better linearity performance in the presence of blockers compared with the first-order TIA.

The LG in the flat region can be estimated by

$$|\mathrm{LG_{flat}}| = A_0 \cdot \frac{\omega_p}{\omega_n} \cdot \sqrt{\frac{R_{\rm IN}C_F}{R_F C_{\rm IN}}} = \frac{\omega_u}{\omega_n} \cdot \sqrt{\frac{R_{\rm IN}C_F}{R_F C_{\rm IN}}}. \tag{12}$$

At first glance, the simplest way to increase the LG in the flat region is by raising ω_u and lowering ω_n. However, enhancing ω_u increases the power consumption, and technology limitations will eventually impose a cap. Additionally, reducing ω_n necessitates a smaller ζ to maintain the same 3-dB bandwidth [see (6)], which can cause stability issues. Therefore, adjusting R and C is a more effective way to increase LG in the flat region. To maintain ζ and ω_n, the feedback and input RC constants (R_FC_F and $R_{\rm IN}C_{\rm IN}$) must remain constant. Since R_F is set by the gain requirement of the RX chain, the only remaining adjustable parameters are $R_{\rm IN}$ and $C_{\rm IN}$. Thus, to increase LG in the flat region while keeping the TIA transfer function constant, $R_{\rm IN}$ must be proportionally increased and $C_{\rm IN}$ reduced. Note that increasing $R_{\rm IN}$ raises the input impedance of the Rauch TIA, which degrades the linearity performance of LNTA. The effect of increasing $R_{\rm IN}$ on the LNTA and RX linearity will be discussed later in this article.

Finally, the first-order TIA and Rauch TIA are simulated in Cadence using the same components used in the simulations presented in Fig. 2. As shown in Fig. 4, a three-stage

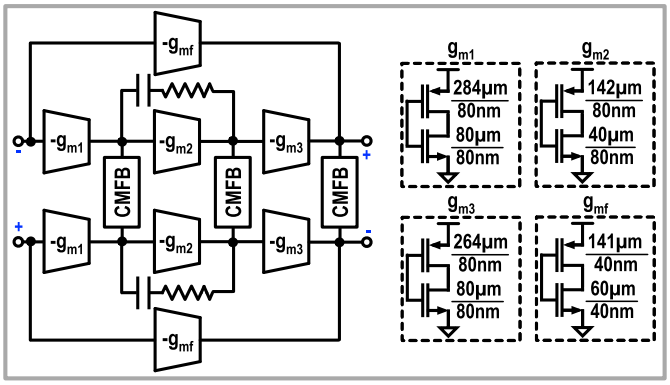

Fig. 4. Schematic of the three-stage OTA.

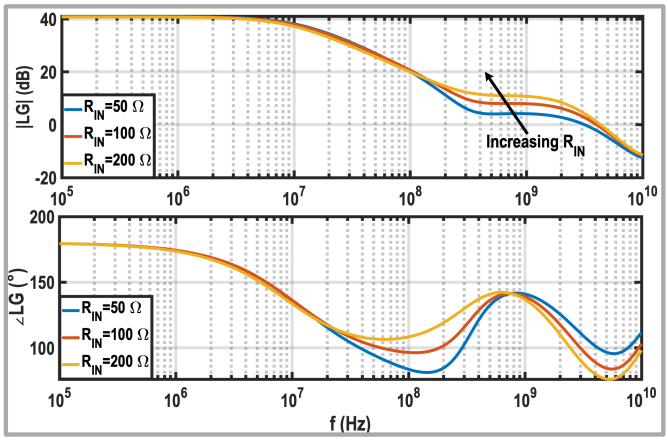

Fig. 5. Simulated LG of the TIA.

operational transconductance amplifier (OTA) is designed as the TIA amplifier to achieve the desired LG and meet the in-band linearity requirements. Following the approach in [36], each stage of the OTA is constructed using inverters, with the detailed sizing of these inverters provided in Fig. 4. Common-mode feedback (CMFB) circuits [41] are placed at the output of each stage to ensure that each inverter is biased near the supply rail midpoint, $\sim V_{\rm DD}/2$. To ensure OTA stability, two compensation techniques are employed: Miller compensation, which sets the dominant pole, and feedforward compensation, which introduces a high-frequency zero to counterbalance the second pole and maintain a sufficient phase margin. The simulated LG of the TIA is depicted in Fig. 5, where the worst phase margin is 73°, and increasing $R_{\rm IN}$ enhances the LG at the bandwidth edge.

Then, two tones (f_1 and f_2) are applied at the input, with the third-order intermodulation term (IM3) falling within the desired band. The first tone (f_1) is placed at the bandwidth edge (i.e., 200 MHz), while the second tone (f_2 is swept across the close-in blocker range. As shown in Fig. 6(a), the Rauch TIA offers 7-dB better linearity performance than the first-order TIA, thanks to its selectivity and higher LG. Moreover, Fig. 6(b) shows the effect of increasing $R_{\rm IN}$ on the linearity performance of the Rauch TIA, resulting in a 5-dB improvement in linearity performance. However, as shown in Fig. 7, the simulated output 1-dB compression point (OP1dB) at the bandwidth edge of the Rauch

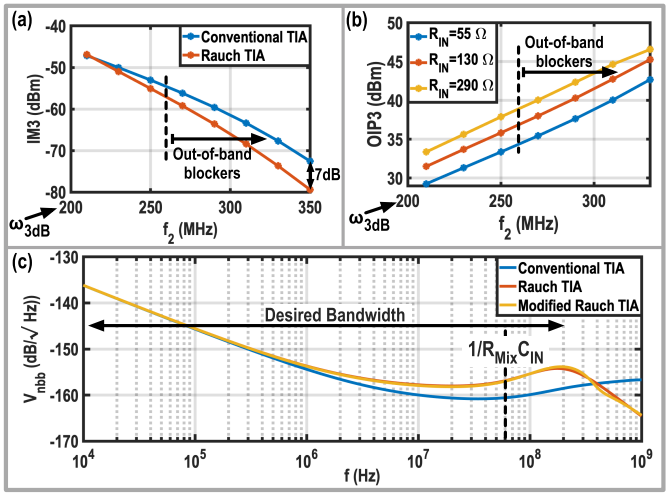

Fig. 6. (a) Comparison between linearity performance of the first-order TIA and Rauch TIA. (b) Effect of increasing R_{IN} and reducing C_{IN} on the linearity performance of the Rauch TIA. (c) Comparison between the output noise of the first-order TIA, conventional Rauch TIA, and the modified Rauch TIA with an active third-order high-pass filter in its feedback.

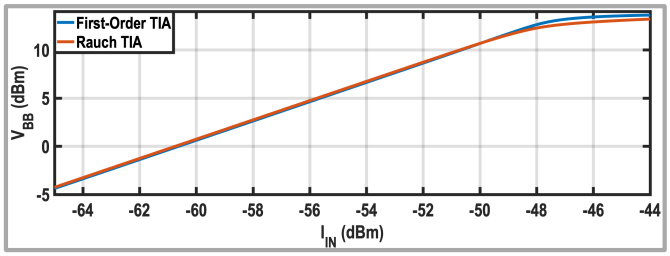

Fig. 7. Simulated OP1dB of the first-order TIA and Rauch TIA at the passband edge.

TIA is slightly lower than first-order TIA (12.6 compared to 13.3 dBm).

D. Performance Over PVT Variations

To evaluate the impact of PVT variations on the performance of the first-order and Rauch TIAs, a Monte Carlo simulation was conducted with global variations across 200 sample points. Since both TIA structures use identical feedback resistors, their transimpedance gains exhibit the same statistical distribution, with a standard deviation of 0.7 dB.

As can be gathered from (1) to (5) and illustrated in the simulation results in Fig. 8(a) and (b), the 3-dB bandwidth of both TIA structures is sensitive to PVT variations. The first-order TIA demonstrates a slightly higher standard deviation in bandwidth (23.9 MHz) compared to the Rauch TIA (21.1 MHz), although both have an average 3-dB bandwidth of approximately 200 MHz. Consequently, calibration is required for both TIAs to maintain the desired 3-dB bandwidth.

To further assess the filtering behavior of Rauch TIA under extreme PVT conditions, four statistical corners were defined based on the highest and lowest bandwidth values observed in the Monte Carlo simulation. Fig. 9 shows the *normalized* transimpedance gain of Rauch TIA to compensate for gain variations across these corners to enhance visualization. As indicated by (4) and confirmed in Fig. 9, the filtering shape

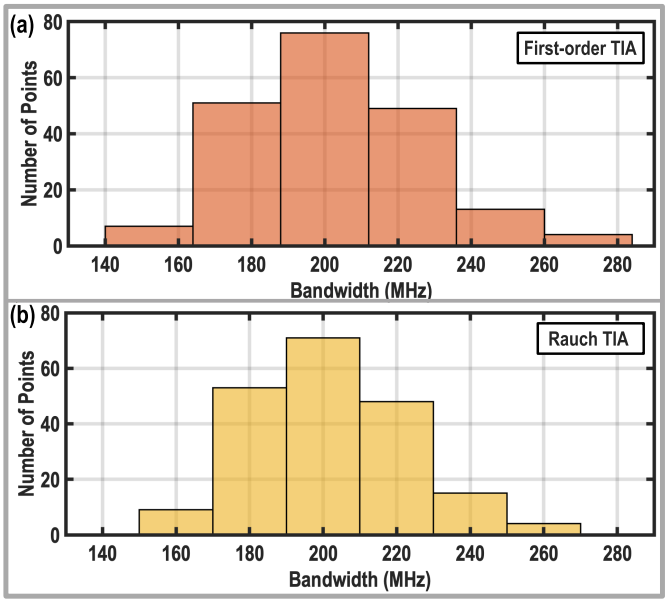

Fig. 8. Monte Carlo simulation results showing the statistical variations in the 3-dB bandwidth of (a) first-order TIA and (b) Rauch TIA.

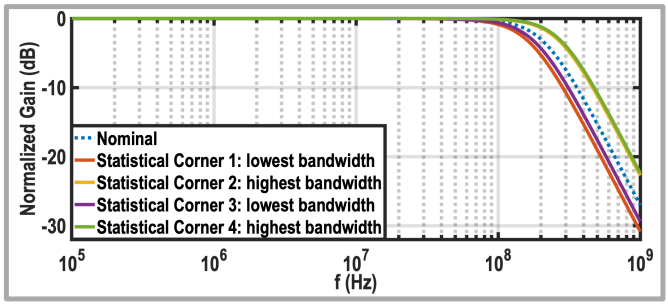

Fig. 9. Normalized transfer function of Rauch TIA under extreme statistical corners.

and slope of Rauch TIA remain largely unaffected by PVT variations since the damping ratio depends on the resistors and capacitors ratios.

E. Noise

In the next step, the output noise of the first-order and Rauch TIAs is estimated and compared. As shown in Fig. 1, the TIA amplifier, R_F, and R_{IN} noise are modeled with $v_{n,A}$, $v_{n,RF}$, and $v_{n,RIN}$, respectively. The output noise of first-order TIA can be calculated as follows:

$$v_{nbb}^2 = v_{n,A}^2 \cdot \left(1 + \frac{R_F}{R_{Mix}} \cdot \frac{sR_{Mix}C_{IN} + 1}{sC_F R_F + 1}\right)^2 + v_{n,RF}^2 \cdot \left(\frac{1}{1 + sC_F R_F}\right)^2. \quad (13)$$

The R_F noise is low-pass filtered and directly appears at the TIA output. The noise transfer function of the TIA amplifier has one zero and one pole. Since the zero created by C_{IN} and R_{Mix} is within the 3-dB bandwidth, the noise of the TIA amplifier increases after the zero frequency. Then, the TIA output noise becomes constant at the bandwidth edge due to the pole formed by R_F and C_F [see simulation results in Fig. 6(c)]. Additionally, the overall TIA output noise improves with a larger R_{Mix}.

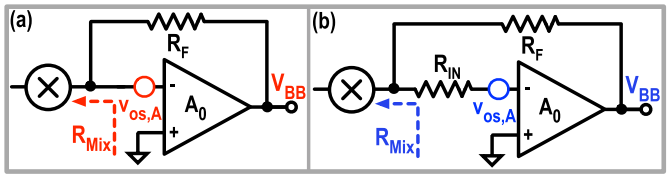

Fig. 10. Simplified model for dc offset analysis of (a) first-order TIA and (b) Rauch TIA.

The output noise of the Rauch TIA is derived as follows:

$$v_{nbb}^2 = v_{n,A}^2 \cdot \left(1 + \frac{R_F}{R_{\text{Mix}}} \cdot \frac{sR_{\text{Mix}}C_{\text{IN}} + 1}{s^2 R_{\text{IN}} C_{\text{IN}} C_F R_F + sC_F R_F \left(1 + \frac{R_{\text{IN}}}{R_F \| R_{\text{Mix}}}\right) + 1}\right)^2 + v_{n,\text{RF}}^2 \cdot \left(\frac{1}{s^2 R_{\text{IN}} C_{\text{IN}} C_F R_F + sC_F R_F \left(1 + \frac{R_{\text{IN}}}{R_F \| R_{\text{Mix}}}\right) + 1}\right)^2 + v_{n,\text{RIN}}^2 \cdot \left(\frac{R_F}{R_{\text{Mix}}} \cdot \frac{sR_{\text{Mix}}C_{\text{IN}} + 1}{s^2 R_{\text{IN}} C_{\text{IN}} C_F R_F + sC_F R_F \left(1 + \frac{R_{\text{IN}}}{R_F \| R_{\text{Mix}}}\right) + 1}\right)^2. \quad (14)$$

Similar to the first-order TIA, the zero formed by C_{IN} and R_{Mix} increases the in-band noise of Rauch TIA. Beyond the bandwidth edge, the noise contributions from all components decrease due to the presence of two complex conjugate poles in their respective noise transfer functions. However, as can be observed in Fig. 6(c), compared to the first-order TIA, the Rauch TIA includes an additional noise source, R_{IN}, which degrades its overall noise performance. Consequently, there is another tradeoff between noise and linearity of the Rauch TIA: increasing R_{IN} improves its LG and in-band linearity but degrades its output noise.

F. DC Offset

In current-mode RXs, the TIA is the primary contributor to overall dc offset performance, making it crucial to analyze the dc offset transfer function for both first-order and Rauch TIA configurations. Fig. 10 shows the simplified model for dc offset calculations, where the TIA amplifier's dc offset is modeled as a voltage source, $v_{\text{os},A}$, and all capacitors are removed, as they act as open circuits at dc. Notably, the dc offset transfer function for both TIAs is the same and can be calculated by

$$\text{dc}_{\text{offset}} = v_{\text{os},A}\left(1 + \frac{R_F}{R_{\text{Mix}}}\right). \quad (15)$$

Therefore, increasing R_{Mix} helps reduce the gain of the TIA amplifier dc offset.

G. Discussion

While the in-band noise of the Rauch TIA is higher than that of the first-order TIA, this issue can be mitigated by utilizing an LNTA to relax the TIA's noise requirements. The Rauch TIA also has a higher input impedance, which could raise concerns about the potential degradation of in-band linearity in LNTA-based RXs. However, as will be demonstrated later in this article, this is not the case. Notably, the Rauch TIA provides better selectivity and higher LG at the bandwidth edge, which are key advantages for handling close-in blockers in 5G applications. Therefore, this work employs Rauch TIA to leverage its superior selectivity and LG characteristics.

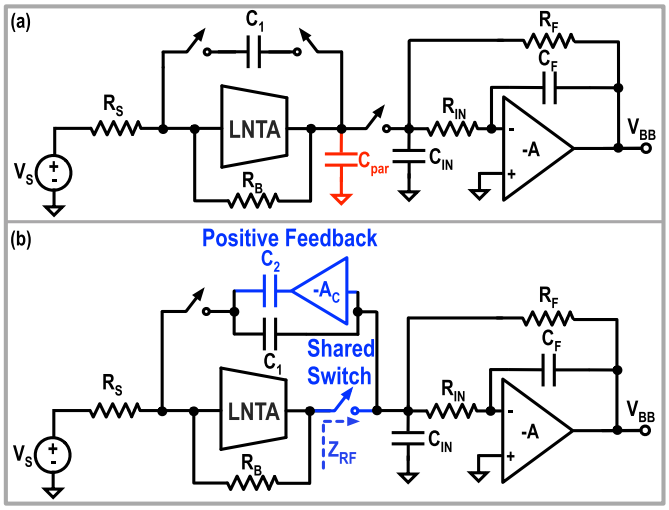

Fig. 11. Current-mode RX utilizes the Rauch TIA with (a) conventional RF front end and (b) proposed RF front end.

III. Proposed RF Front End

As can be gathered from (10) and (11), the TIA LG is limited by the impedance observed from the baseband port of passive mixers toward the RF front end, denoted R_{Mix}. In mixer-first RXs, R_{Mix} is constrained by both the antenna impedance (50 Ω) and the large parasitic capacitors of passive mixers. To address this, we incorporate an LNTA that offers a higher output impedance than the antenna and alleviates parasitic capacitance at the LNTA output by allowing for reduced sizes of the down-converting passive mixers.

A. Expanding RX Operating Frequency

Fig. 11(a) presents a preliminary block diagram of the proposed RX consisting of an LNTA and the Rauch TIA. An N-path notch filter is placed in the LNTA feedback to achieve RF selectivity at the RX input [18], [19], [20], [21], [22], [23], [24], [25], [26], [27], [28], [29], [30], [31], [32]. However, two switch sets at the LNTA output—one for the N-path notch filter and another for the down-converting passive mixers—increase the total parasitic capacitance at the LNTA output (denoted as C_{par}). This parasitic capacitance, in combination with the LNTA output resistance, creates a pole that limits the operating frequency of prior-art LNTA-based RXs to below 6 GHz [18], [19], [20], [21], [22], [23], [24], [25], [26], [27], [28], [29], [30], [31], [32]. To enhance the RX operating frequency, Fig. 11(b) combines the two switch sets into one [42], [43], reducing C_{par} and allowing the pole to shift beyond 8 GHz.

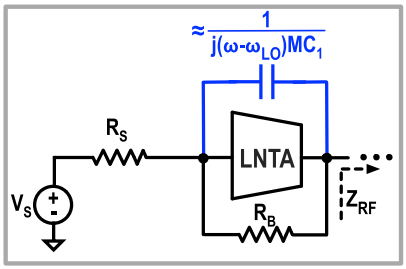

Fig. 12. Equivalent model of the RF front end of the preliminary RX structure in Fig. 11(a).

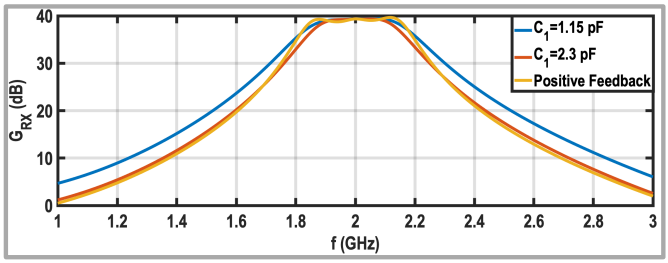

Fig. 13. Comparing the RX far-out front-end rejection. Blue and red curves are simulated using the conventional structure with an N-path notch filter in the LNTA feedback, and the orange one employs the proposed structure.

B. 3-dB Bandwidth Expansion

The 3-dB bandwidth of the preliminary RX structure in Fig. 11(a) is limited at its input node. Due to the transparency of passive mixers, the capacitors in the N-path notch filter are upconverted to the RF domain. As a result, the N-path notch filter can be modeled as a bandpass-shaped impedance in the RF domain, as illustrated in Fig. 12 and discussed in [20]. Therefore, the RX input bandwidth is governed by the Miller effect of N-path notch filter (C_{Miller}) and the antenna resistance (R_S), which can be estimated as follows:

$$\text{BW}_{\text{RF}} = \frac{2}{R_S C_{\text{Miller}}} \approx \frac{2}{R_S A_{v,\text{LNTA}} M C_1} \tag{16}$$

where C_1 and M represent the unit capacitor of the N-path notch filter and the number of the local oscillator (LO) phases, respectively. $A_{v,\text{LNTA}}$ is the LNTA voltage gain and can be approximated by $G_m Z_{\text{RF}}(f)$, where G_m is the LNTA's transconductance and $Z_{\text{RF}}(f)$ is its load. For 5G NRs, the RF bandwidth reaches up to 400 MHz for operating frequencies above 3 GHz, necessitating a reduction in C_1 to increase the bandwidth. However, simulation results in Fig. 13 show that reducing C_1 from 2.3 to 1.15 pF to boost the RF bandwidth from 200 to 400 MHz leads to a 4-dB degradation in out-of-band rejection at a specific far-out offset frequency from the LO frequency. This degradation may impact RX performance in base station co-location applications where a −4-dBm blocker is present.

This work leverages the bandpass-shaped input impedance of the Rauch TIA to enhance the RF bandwidth without compromising the out-of-band rejection and linearity. To achieve this, a positive feedback branch, consisting of an amplifier (A_c) and a series capacitor (C_2), is introduced in parallel with C_1, as depicted in Fig. 11(b). This technique modifies the Miller capacitor at the RX input to

$$C_{\text{Miller}} = M \cdot \Big((1 + G_m Z_{\text{RF}}(f)) C_1 + (1 - G_m Z_{\text{RF}}(f) A_C) C_2 \Big). \tag{17}$$

At low baseband frequencies, the input impedance of Rauch TIA is R_F/A_0, which effectively reduces Z_{RF} and undermines the impact of positive feedback. Hence, as shown in Fig. 14, the equivalent Miller capacitor is at its maximum, $M(C_1 + C_2)$. As the frequency increases, the input impedance of the Rauch TIA starts to rise toward R_{IN}, enhancing the effect of the positive feedback path. At the passband edges, Z_{RF} can be approximated by R_{IN}/M, leading to the following

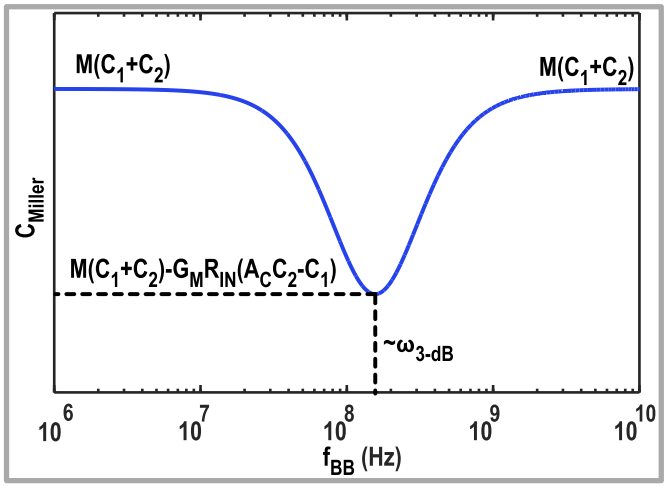

Fig. 14. Effective Miller capacitor versus the baseband frequency.

approximation for the Miller capacitor:

$$C_{\text{Miller}} = M \times (C_1 + C_2) - G_m R_{\text{IN}}(A_c C_2 - C_1). \tag{18}$$

Therefore, as shown in Fig. 14, the proposed positive feedback structure reduces the Miller capacitance at the bandwidth edge, thus flattening the RX in-band response and expanding the RX bandwidth. At out-of-band frequencies, as can be inferred from (9), the input impedance of the Rauch TIA decreases due to the presence of its poles, which diminishes the effect of the proposed positive feedback. As a result, the Miller capacitance increases at far-out frequencies, returning to $M(C_1 + C_2)$. This behavior enhances the out-of-band rejection and improves the filtering roll-off of the proposed RX. Fig. 13 demonstrates that compared to the conventional structure, the proposed positive feedback effectively boosts the 3-dB bandwidth, flattens the in-band response, increases roll-off, and maintains out-of-band rejection. Additionally, the noise and linearity requirements for the added amplifiers are relaxed, as their inputs are connected to the TIA virtual ground, and their noise experiences bandstop filtering when appearing at the RX output.

C. Impact of PVT-Induced A_c Variations on RX Stability

As can be gathered from (18), an increase in the gain of the positive feedback amplifier, A_c, due to PVT variations can cause the Miller capacitance to become negative at the bandwidth edges, potentially leading to stability issues. To evaluate this, the amplifier gain, implemented with a self-biased inverter, was simulated under various PVT conditions,

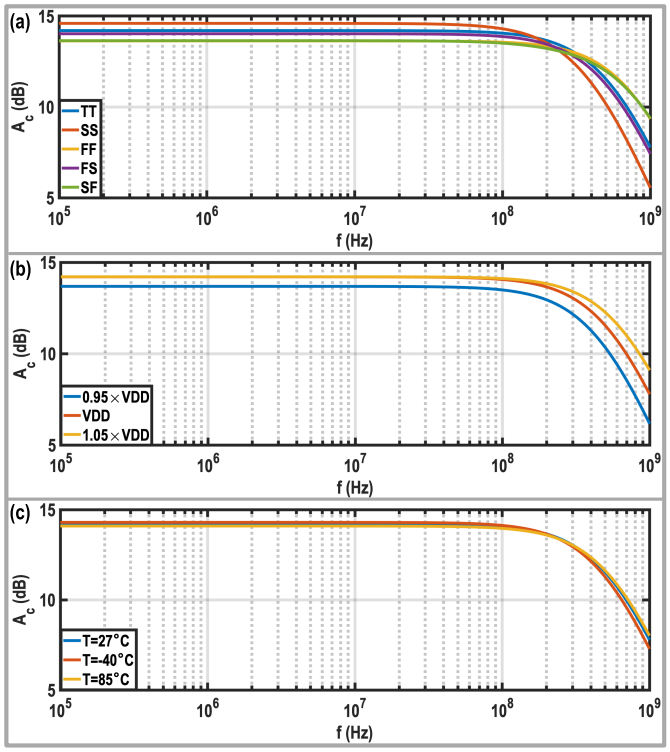

Fig. 15. Gain of positive feedback amplifier across (a) process, (b) supply, and (c) temperature variations.

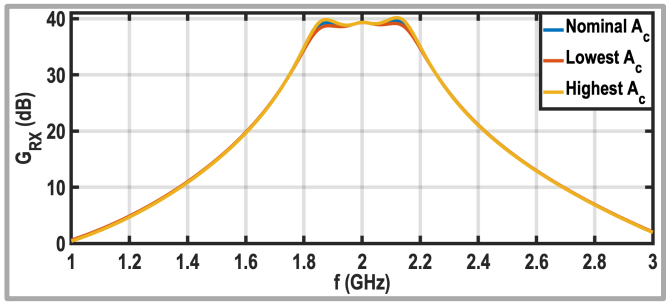

Fig. 16. Simulated RX gain for the worst case scenarios of A_c.

as shown in Fig. 15. For the nominal corner, the simulated gain is 14.2 dB, with a 3-dB bandwidth exceeding 500 MHz. The PVT-induced gain variation is limited to ±0.6 dB, as PVT variations affect both transconductance and output resistance in opposing directions, keeping the overall gain stable.

To evaluate worst case scenarios, A_c was intentionally varied by ±1.8 dB in the RX chain gain simulations. As shown in Fig. 16, these variations result in only ±0.6-dB change in RX gain peaking. Thus, PVT-induced variations in A_c do not cause stability issues. Moreover, the resulting RX gain peaking can easily be compensated by adjusting C_2.

IV. RX In-Band Linearity

In this section, we analyze the in-band linearity of the proposed receiver. Fig. 17 presents a simplified RX model, which consists of three cascaded blocks: the LNTA (L), the passive mixers (P), and the TIAs (T). Note that the on-resistance and nonlinearity of the passive mixers are neglected in this analysis, as the LNTA and TIAs are considered the primary

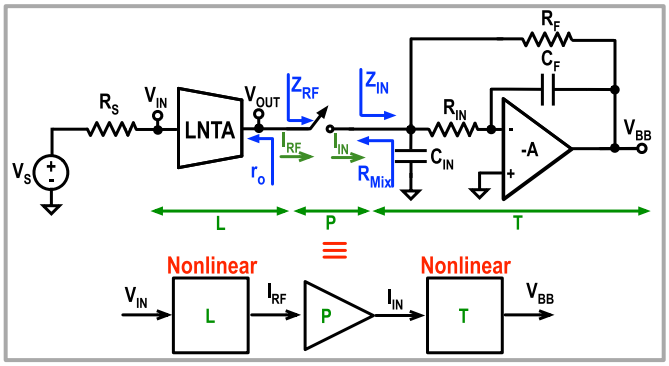

Fig. 17. Simplified model of the proposed RX for in-band linearity analysis.

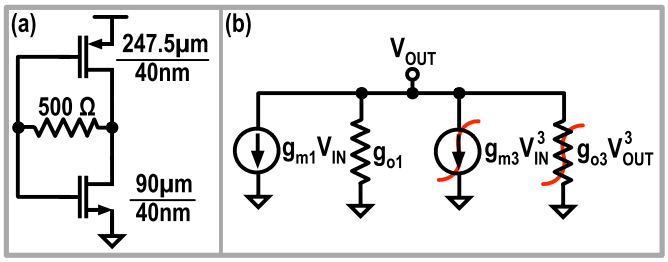

Fig. 18. (a) Transistor-level implementation of the LNTA. (b) Small-signal model of the LNTA.

sources of nonlinearity. Moreover, since the in-band linearity is analyzed in this section, the nonlinearity of LNTA and TIAs is assumed to be frequency-independent across the desired bandwidth. We will first analyze the nonlinearity of the LNTA and TIAs individually, following the methodology established in [44]. Subsequently, we will calculate the overall nonlinearity of the RX chain.

A. Low-Noise Transconductance Amplifier

The LNTA has two main nonlinearity sources: the nonlinearity of its transconductance and its output resistance. Assuming a cubic relationship between the LNTA output voltage and the input voltage ($V_{\rm IN}$), the LNTA output current ($I_{\rm RF}$) can be derived by applying Kirchhoff's current law (KCL) at the LNTA output. By neglecting higher order harmonics, we obtain

$$I_{\rm RF} = -\frac{r_o}{Z_{\rm RF}+r_o}\cdot g_{m1}V_{\rm IN} - \frac{r_o}{Z_{\rm RF}+r_o}\left(g_{m3}+g_{o3}(g_{m1}Z_L)^3\right)V_{\rm IN}^3 \quad (19)$$

where g_{m1} and r_o are the equivalent LNTA's transconductance and output resistance, respectively, while $Z_L = r_o \| Z_{\rm RF}$ is the LNTA's load. Moreover, as illustrated in Fig. 18(b), g_{m3} and g_{o3} correspond to the third-order nonlinearity of the LNTA's transconductance and output conductance, respectively.

As inferred from (19) and discussed in [45], the nonlinearity of $Z_{\rm RF}$ may induce nonlinear RF-domain current at the LNTA output. At low offset frequencies, $Z_{\rm RF}$ is significantly smaller than r_o, making the nonlinear current contribution of $Z_{\rm RF}$ negligible. As the offset frequency increases, the input impedance of the Rauch TIA approaches $R_{\rm IN}$, which is linear and almost independent of the TIA amplifier's nonlinearity. Consequently, the input impedance of the Rauch TIA does

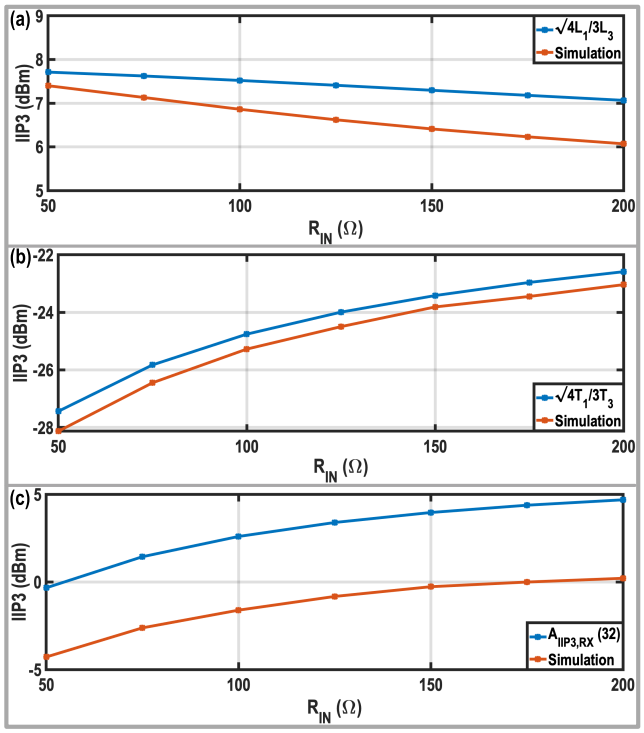

Fig. 19. Simulated and calculated in-band linearity of (a) LNTA, (b) TIA, and (c) proposed RX.

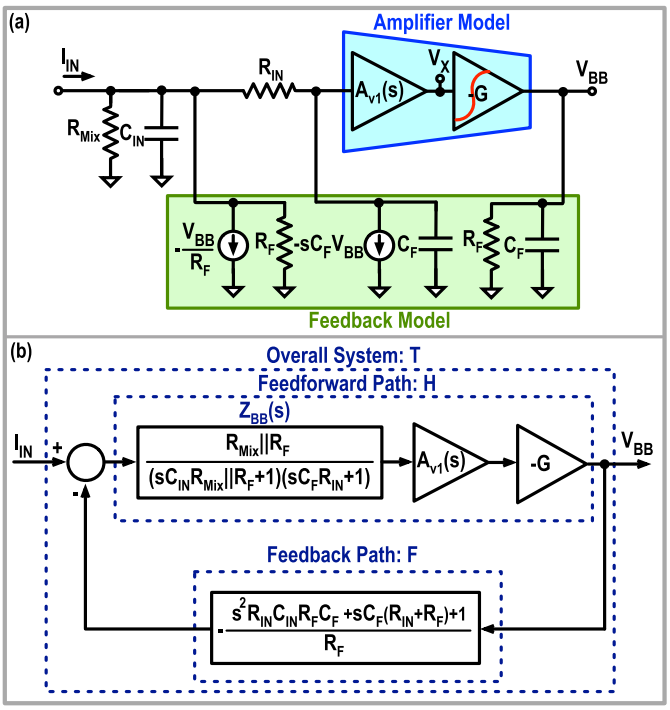

Fig. 20. (a) Simplified schematic of the Rauch TIA to account for R_F and C_F loading effects. (b) Equivalent approximated model of the Rauch TIA.

not induce nonlinear RF current, leaving the nonlinearity of the LNTA as the dominant source of nonlinear RF current.

The first- and third-order Volterra kernel transforms can then be derived as

$$L_1(j\omega_1) = -\frac{r_o}{Z_{\mathrm{RF}}(j\omega_1)+r_o}\cdot g_{m1} \tag{20}$$

$$L_3(j\omega_1, j\omega_2, j\omega_3) = -\frac{r_o}{Z_{\mathrm{RF}}(j\omega_1+j\omega_2+j\omega_3)+r_o} \cdot \Big(g_{m3}+g_{o3}\cdot(g_{m1}Z_L(j\omega_1))\cdot(g_{m1}Z_L(j\omega_2)). \cdot(g_{m1}Z_L(j\omega_3))\Big) \tag{21}$$

where L_1 and L_3 represent the linear and third-order nonlinear terms, respectively. When two in-band tones with amplitudes of A and frequencies of ω_1 and ω_2 are applied to the RX input, the third-order IM3 tones in the LNTA output current occur at $2\omega_1-\omega_2$ and $2\omega_2-\omega_1$. Using (21), the amplitude of IM3 tones can be calculated as $3/4A^3|L_3(j\omega_1, j\omega_1, -j\omega_2)|$ and $3/4A^3|L_3(j\omega_2, j\omega_2, -j\omega_1)|$. The IIP3 of the LNTA is then estimated by $(4L_1/3L_3)^{1/2}$.

As shown in Fig. 18(a), the LNTA is implemented using a self-biased inverter with low-voltage threshold (LVT) devices of minimum channel length to minimize parasitic capacitance at the RX input. A 500-Ω shunt resistive is also used to bias the transistors in saturation. By sweeping the input and output voltages, the output current variation is simulated to estimate the transconductance and output conductance nonlinearity. The resulting linearity parameters are summarized in Table I. The values of g_{m3} and $g_{o,3}$ are then used to calculate the LNTA's IIP3. Fig. 19(a) shows the simulated and estimated IIP3 of LNTA at the bandwidth edge versus R_{IN}, in which

TABLE I
SUMMARY OF EXTRACTED LINEARITY PARAMETERS OF LNTA AND TIA AMPLIFIER LAST STAGE

LNTA	g_{m1}	g_{m3}	g_{o1}	g_{o3}
	125 m	270 m	16 m	1 m
TIA Amplifier Last Stage	g_{mt1}	g_{mt3}	g_{ot1}	g_{ot3}
	20 m	20 m	1 m	0.1 m

increasing R_{IN} from 50 to 200 Ω results in only a ≈1.3-dB IIP3 degradation.

B. Transimpedance Amplifier

Next, the nonlinearity of the Rauch TIA is analyzed by decomposing the TIA (T) into two main components: the feedforward path (H) and the feedback path (F), as outlined in [44]. As shown in Fig. 20(a), to calculate H, F, and T, the amplifier and feedback impedance are modeled as follows. The feedback current is represented with two current sources at the TIA input, while R_F and C_F are placed at the TIA input and output to account for their loading effects. Additionally, the TIA amplifier is also modeled with two cascade stages: A_{v1} and G. A simplified system model of the Rauch TIA is then developed, as illustrated in Fig. 20(b). Using this model, we first calculate the Volterra kernel transforms of the feedforward and feedback paths and finally derive the Volterra kernel transforms of the overall TIA.

1) Feedforward Path: Miller compensation is usually used within A_{v1} for stability purposes, setting the dominant pole of the TIA amplifier, ω_p. A_{v1} is frequency-dependent for in-band signals since $\omega_p < \omega_{3\,\mathrm{dB}}$, as discussed earlier. However, due to the low-voltage swing at the TIA input, A_{v1} remains linear

and does not contribute to TIA nonlinearity. Furthermore, R_F and C_F have negligible loading effects on G, making G frequency independent for the in-band signals. Because of the large voltage swing at the TIA output, G is the primary source of nonlinearity in the TIA, with two main nonlinearities stemming from its transconductance and output resistance. The Volterra kernel transforms of G can be calculated using the same procedure used for the LNTA

$$G_1 = -g_{mt1} r_{ot1} \tag{22}$$

$$G_3 = -\left((g_{mt1} r_{ot1})^3 g_{ot3} + g_{mt3}\right) r_{ot1} \tag{23}$$

where g_{mt1} (g_{mt3}) and g_{ot1} (g_{ot3}) represent the linear (third-order nonlinearity) components of the transconductance and output conductance of the amplifier's final stage, respectively, considering a small-signal nonlinearity model similar to that shown in Fig. 18(b). Considering the model in Fig. 20(b), the Volterra kernel transforms of the feedforward path are calculated using (22) and (23)

$$H_1(j\omega) = -G_1 A_{v1}(j\omega) Z_{\mathrm{BB}}(j\omega) \tag{24}$$

$$\begin{aligned} H_3(j\omega_1, j\omega_2, j\omega_3) = &-G_3(j\omega_1, j\omega_2, j\omega_3) \\ &\cdot A_{v1}(j\omega_1) Z_{\mathrm{BB}}(j\omega_1) A_{v1}(j\omega_2) \\ &\cdot Z_{\mathrm{BB}}(j\omega_2) A_{v1}(j\omega_3) Z_{\mathrm{BB}}(j\omega_3) \end{aligned} \tag{25}$$

where $Z_{\mathrm{BB}}(s)$ is defined by

$$Z_{\mathrm{BB}}(j\omega) = \frac{R_F \| R_{\mathrm{Mix}}}{(j\omega R_F \| R_{\mathrm{Mix}} C_{\mathrm{IN}} + 1)(j\omega R_{\mathrm{IN}} C_F + 1)}. \tag{26}$$

2) Feedback Path: Since the feedback path only consists of passive elements, it is linear and does not contribute to the TIA's nonlinearity. Therefore, the third-order Volterra kernel transform of the feedback path is 0, and its first-order Volterra kernel transform is

$$F_1(j\omega) = -\frac{-\omega^2 R_{\mathrm{IN}} C_{\mathrm{IN}} R_F C_F + j\omega(R_{\mathrm{IN}} + R_F) C_F + 1}{R_F}. \tag{27}$$

3) Overall TIA: To calculate the Volterra kernel transforms of the TIA, the gain reduction factor of the TIA loop must first be derived

$$R(j\omega) = -\frac{1}{1 + H_1(j\omega) F_1(j\omega)} = -\frac{1}{1 + \mathrm{LG}(j\omega)} \tag{28}$$

where LG is given by (11). The first-order Volterra kernel transform of the Rauch TIA is

$$T_1(j\omega) = H_1(j\omega) R(j\omega) = \frac{H_1(j\omega)}{1 + H_1(j\omega) F_1(j\omega)}. \tag{29}$$

Assuming that the TIA amplifier has a high voltage gain, (29) simplifies to $1/F_1(j\omega)$, as given in (3). Finally, the third-order Volterra kernel transform of the Rauch TIA can be derived as follows:

$$\begin{aligned} T_3(j\omega_1, j\omega_2, j\omega_3) = &\, R(j\omega_1) R(j\omega_2) R(j\omega_3) \\ &\cdot H_3(j\omega_1, j\omega_2, j\omega_3) \\ &\cdot R(j\omega_1 + j\omega_2 + j\omega_3). \end{aligned} \tag{30}$$

When two input currents at ω_1 and ω_2 are applied to the TIA input, two IM3 tones are generated at $2\omega_1 - \omega_2$ and $2\omega_2 - \omega_1$. Assuming that the input current amplitude is I, the IM3 tones have amplitudes of $3/4 I^3 |T_3(j\omega_1, j\omega_1, -j\omega_2)|$ and $3/4 I^3 |T_3(j\omega_2, j\omega_2, -j\omega_1)|$. After replacing (28) into (30), the third-order Volterra kernel transform for the in-band IM3 tone $(2\omega_1 - \omega_2)$ can be recalculated

$$\begin{aligned} &T_3(j\omega_1, j\omega_2, j\omega_3) \\ &= \frac{1}{1 + \mathrm{LG}(j\omega_1)} \cdot \frac{1}{1 + \mathrm{LG}(j\omega_1)} \cdot \frac{1}{1 + \mathrm{LG}(-j\omega_2)} \\ &\quad \cdot H_3(j\omega_1, j\omega_2, j\omega_3) \cdot \frac{1}{1 + \mathrm{LG}(j\omega_1 + j\omega_1 - j\omega_2)}. \end{aligned} \tag{31}$$

Thus, enhancing the LG at the frequencies of the blockers and IM3 tones improves the in-band linearity performance of the TIA.

Similar to the LNTA, the values of g_{mt3} and g_{ot3} for the TIA are estimated by monitoring the output current of the last stage of the Rauch TIA while sweeping its input and output voltages. The simulated results are summarized in Table I. These values are used to calculate the TIA's IIP3. Fig. 19(b) shows the simulated and estimated IIP3 of TIA at the bandwidth edge versus R_{IN}, where increasing R_{IN} from 50 to 200 Ω improves IIP3 by 5 dB, aligning well with IIP3 calculations ($(4T_1/3T_3)^{1/2}$). Note that the values of R_F, C_{IN}, C_F, and R_{IN} are similar to those used in Fig. 2 with C_F slightly adjusted for 3-dB bandwidth tuning.

C. RX Chain

As mentioned earlier, the entire RX chain can be viewed as a cascade of the LNTA, passive mixers, and TIAs (see L, P, and T in Fig. 17). P is a linear gain block, and the differential gain of the passive mixers is $2/M \mathrm{sinc}(1/M)$. Thus, I_{IN} in Fig. 20(a) equals $2/M \mathrm{sinc}(1/M) I_{\mathrm{RF}}$. Considering this point, the IIP3 of the RX chain ($A_{\mathrm{IIP3,RX}}$) can be calculated as follows [46]:

$$\frac{1}{A^2_{\mathrm{IIP3,RX}}} = \frac{1}{A^2_{\mathrm{IIP3,LNTA}}} + \frac{\left(\frac{2}{M}\mathrm{sinc}\left(\frac{1}{M}\right) L_1\right)^2}{A^2_{\mathrm{IIP3,TIA}}} \tag{32}$$

where $A_{\mathrm{IIP3,LNTA}}$ and $A_{\mathrm{IIP3,TIA}}$ are the IIP3 of the LNTA and TIA, respectively. Fig. 19(c) shows the simulated IIP3 of the RX chain where increasing R_{IN} enhances the IIP3 by 4 dB, which closely matches the 5-dB improvement predicted by (32). However, a 3.8-dB discrepancy exists between the simulated and calculated RX IIP3 values. To simplify our analysis, we neglected the second-order nonlinearity of the TIA and LNTA. This decision is based on the fact that the TIA functions as a pseudo-differential circuit, while the LNTA is implemented using a single inverter-based amplifier, where the second-order nonlinearity can be minimized through careful sizing of the nMOS and pMOS devices [47]. However, it is important to note that the second-order nonlinearity is not completely eliminated. As discussed in [44], the interaction between the second-order nonlinearities of two cascaded blocks contributes to third-order nonlinearities, leading to a mismatch between the calculated and simulated IIP3 values. One approach to mitigate the second-order distortion is to add an ac coupling capacitor between the LNTA and the passive mixers. This capacitor would allow the signals at the operating frequency to pass through while blocking the second-order intermodulation (IM2) tones at lower frequencies. Simulation results show that adding this capacitor improves the in-band linearity of the RX by approximately 2 dB, bringing the simulation results closer to the calculated values. However,

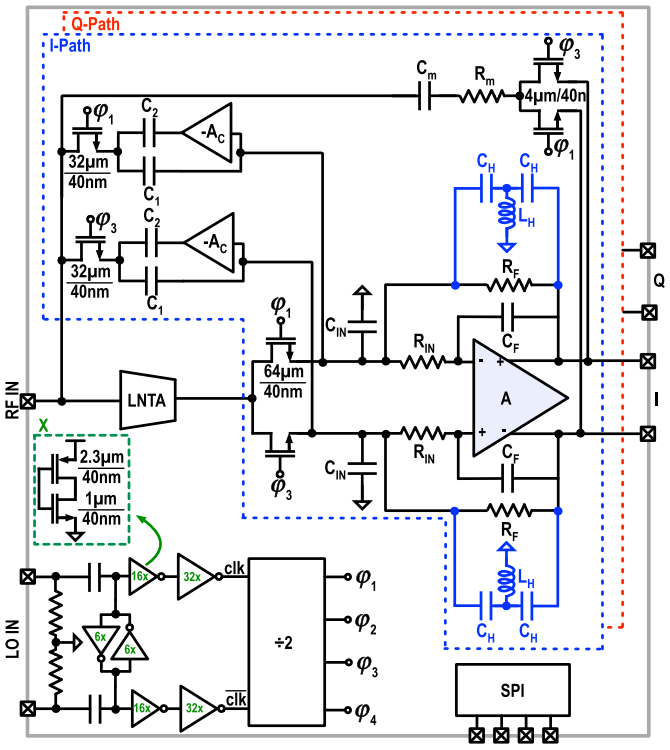

Fig. 21. Proposed RX block diagram.

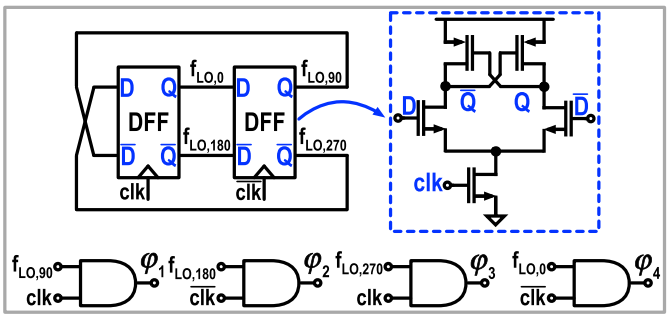

Fig. 22. Schematic of LO generation block.

TABLE II
TUNABLE RANGE OF THE UTILIZED KEY COMPONENTS OF THE PROPOSED RX

C_1	C_2	C_{IN}	R_{IN}	C_F	R_F
2.3-9.2 pF	0.19-1.5 pF	2.3-34.4 pF	50-200 Ω	0.24-1.44 pF	0.4-1.6 kΩ

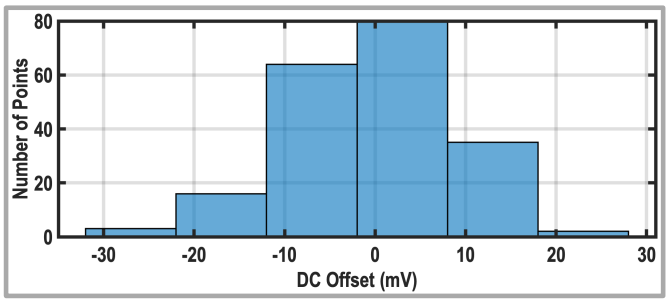

Fig. 23. Monte Carlo simulation results of dc offset at the RX output.

to pass the desired signals at the lowest operational frequency of 0.4 GHz, the ac coupling capacitor would need to be relatively large. This would introduce significant parasitic capacitance at the LNTA output, which could degrade the RX's operating frequency and noise performance. Consequently, despite the resulting degradation in linearity, we chose not to include this capacitor in the design in order to preserve the operating frequency.

D. Discussion

In this section, we analyzed the impact of increasing R_{IN} and reducing C_{IN} on the linearity performance of the RX. An increase in R_{IN} degrades the in-band linearity of the LNTA but improves the in-band linearity of the Rauch TIA. Since the RX's overall in-band linearity is mainly limited by the Rauch TIA, increasing R_{IN} enhances the RX's overall linearity. However, it is important to note that in advanced CMOS technologies with supply voltages below 1 V, the nonlinearity degradation of the LNTA could dominate, potentially outweighing the improvement achieved in the Rauch TIA.

V. CIRCUIT IMPLEMENTATION

Fig. 21 shows the complete block diagram of the proposed RX. All key parameters of the proposed RX (C_1, C_2, C_{IN}, R_{IN}, C_F, and R_F) are tunable and can be controlled via the serial peripheral interface (SPI). The tunable ranges for these parameters are summarized in Table II.

The input signal is converted into an RF current by the LNTA, which is then down-converted by four-phase passive mixers, and the TIAs eventually convert it to baseband voltages to generate in-phase (I) and quadrature (Q) signals. To achieve input matching, the output voltages from the TIAs are upconverted to the RF domain, combined, and then applied to the RF input of the RX via the matching resistor and capacitor (R_m and C_m). A -1 multiplication in the translational feedback network ensures the stability of the input matching loop [48]. The passive mixers are implemented using nMOS transistors, with their dimensions shown in Fig. 21. Additionally, similar to the LNTA in Fig. 18(a), the positive feedback amplifier is realized with a compact self-biased inverter. However, smaller devices are employed in the positive feedback amplifier (pMOS: 9.4 μm/40 nm and nMOS: 4 μm/40 nm) to reduce power consumption. A 10-kΩ feedback resistor is used to bias the amplifier and slightly attenuate its gain, preventing stability issues. At the in-band frequencies, the series capacitor (C_2 in Fig. 21) presents a high impedance, ensuring that the noise and nonlinearity of the positive feedback amplifier do not degrade the RX performance.

Fig. 22 shows the simulated dc offset of the proposed RX using PSS analysis in cadence. The simulated standard deviation of dc offset is 9.2 mV at the RX output. Due to the relatively low dc offset, analog domain cancellation is unnecessary. While it may slightly reduce the dynamic range of the off-chip analog-to-digital converter (ADC), dc offset cancellation can be efficiently handled in the digital domain.

In the proposed RX, a differential off-chip LO signal is first buffered and then passed through a divide-by-two stage to generate the four-phase non-overlapping LOs. The detailed schematic of LO generation block is shown in Fig. 23. Two cascaded flip-flops [20] are utilized to generate four 50% duty cycle clocks. These clocks are then resampled with the

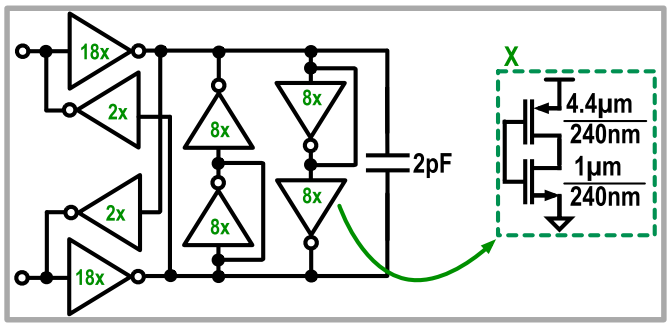

Fig. 24. Active implementation of the differential inductor.

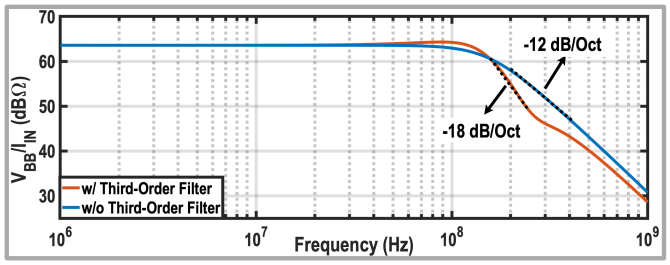

Fig. 25. Filtering response of Rauch TIA before and after adding the third-order impedance.

buffered input clocks to produce 25% non-overlapping LOs, which drive the passive mixers.

As mentioned earlier, one of the main challenges in 5G applications is the presence of close-in blockers, which necessitate sharp filtering. In this work, a third-order high-pass filter is placed in parallel with the R_F to further increase the selectivity of the Rauch TIA (highlighted in blue in Fig. 21). To implement the baseband inductors for the high-pass filter, the ground ports of the inductors, driven by complementary LOs, are connected and replaced with a single inductor. The resulting inductor is realized using a gyrator with a capacitor load, as shown in Fig. 24. The inverters in the active inductor are implemented using large-channel devices to minimize the undesired series resistance of the active inductor [33]. Like Nauta's cell [49], four extra inverters are used at the gyrator output to ensure the transistors remain in saturation. Fig. 25 shows that the TIA's transition slope increases to −18 dB/oct with the third-order high-pass filter. However, due to the limited bandwidth of the gyrator, the filtering order reduces to second-order at far-out offset frequencies. Note that the nonlinearity and noise generated by the active inductor appear at the TIA output after undergoing high-pass filtering, which helps relax its noise and linearity requirements. To assess this effect, two RX schematics were simulated in Cadence: one with the active inductor and the other with an ideal inductor. Two in-band tones were applied to the RX ($f_1 = f_{LO} + f_{IF}$ and $f_2 = f_{LO} + f_{IF} - 10$ MHz), with f_{IF} swept across the 3-dB bandwidth. As shown in Fig. 26, the degradation in in-band linearity is minimal throughout most of the bandwidth, with only a 0.2-dB reduction at the bandwidth edge. Additionally, as illustrated in Fig. 6(c), the active inductor causes a 0.5-dB increase in the output noise of the Rauch TIA.

VI. Measurement Results

The proposed RX is implemented in TSMC 40-nm Bulk CMOS technology. Fig. 27 shows the die micrograph of

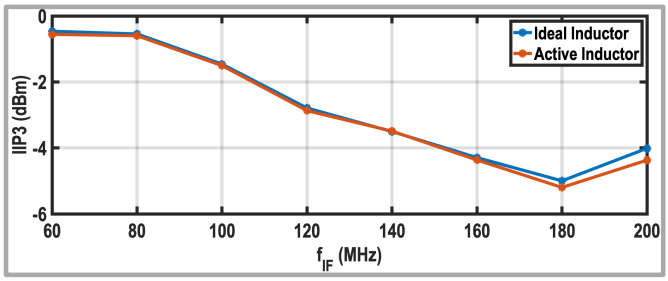

Fig. 26. Effect of the active inductor on the simulated RX in-band IIP3.

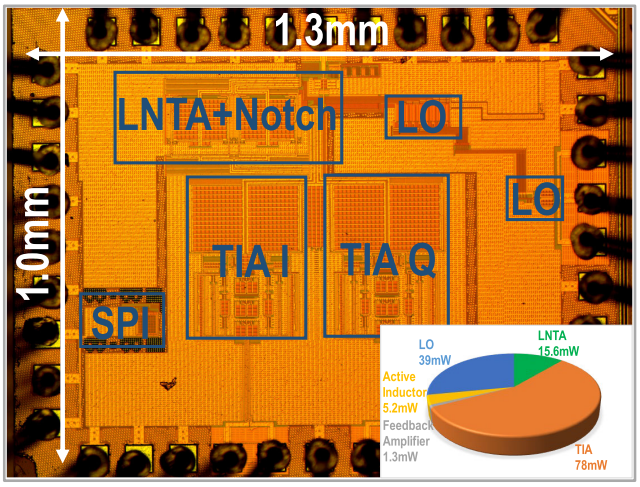

Fig. 27. Die micrograph and power consumption breakdown at $f_{LO} = 3$ GHz.

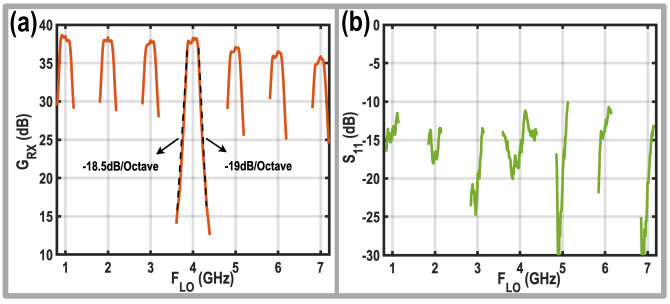

Fig. 28. Measured (a) gain and (b) in-band S_{11} over the operating frequency.

the proposed RX, with the chip's core area and active area measuring 1.3 and 0.4 mm^2, respectively. The RX consumes between 105.2 and 194.9 mW from a 1.3-V supply while operating over a frequency range of 0.4–7.3 GHz. The power consumption breakdown at 3 GHz LO frequency (f_{LO}) is depicted in Fig. 27.

Fig. 28(a) shows the measured gain versus the operating frequency, with a gain of 38.5 dB at low LO frequencies and 35.8 dB at high LO frequencies. Due to the parasitic capacitors, the measured RF bandwidth is about 300 MHz, compared to the desired 400 MHz. The filtering order of the proposed RX is better than −60 dB/dec. Fig. 28(b) shows the measured in-band S_{11}, which remains below −10 dB across the 3-dB bandwidth and operating frequency. The measured NF, shown in Fig. 29(a), is 3.2 dB at $f_{LO} = 1$ GHz and increases to 5.8 dB at $f_{LO} = 7$ GHz. The measured LO leakage is −80 dBm at the lowest LO frequency and increases to −50 dBm at the highest LO frequency, as shown in Fig. 29(b).

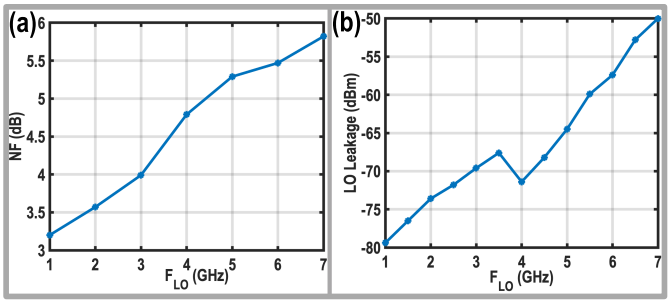

Fig. 29. Measured (a) NF and (b) LO leakage across the operating frequency.

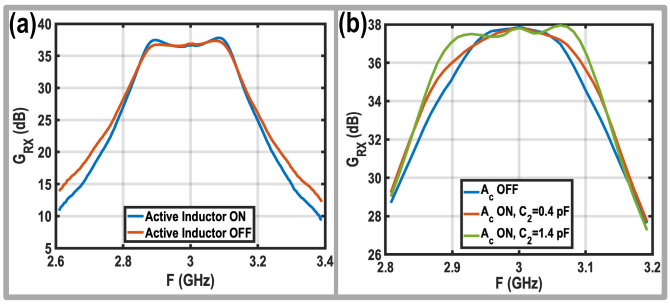

Fig. 30. (a) Effect of the third-order impedance on the selectivity of the proposed RX. (b) Extending the measured 3-dB bandwidth with the proposed positive feedback.

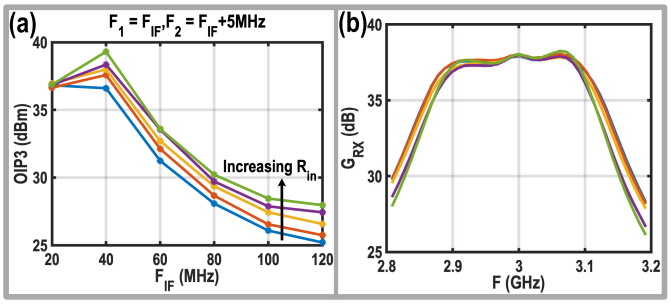

Fig. 31. (a) Improving the measured in-band OIP3 by increasing R_{IN} and reducing C_{IN}. (b) Impact of increasing R_{IN} and reducing C_{IN} on the RX in-band gain transfer function.

Fig. 30(a) highlights the impact of the third-order high-pass filter on the selectivity of the proposed RX, where enabling the active inductor improves the RX selectivity by -10 dB/dec. As demonstrated in the measured results shown in Fig. 30(b), activating the positive feedback amplifier (A_c) and adjusting the value of C_2 increases the RX bandwidth without sacrificing the far-out out-of-band rejection.

Fig. 31(a) presents the measured in-band linearity. Two tones at $f_1 = f_{\mathrm{IF}}$ and $f_2 = f_{\mathrm{IF}} + 5$ MHz are applied to the RX input, with f_{IF} swept across the 3-dB bandwidth. The measured in-band OIP3 is approximately 38 dBm when f_{IF} is below 40 MHz. Due to the limited bandwidth of the LG, the in-band linearity starts to degrade at $f_{\mathrm{IF}} = 40$ MHz, reaching 27 dBm near the 3-dB bandwidth. Furthermore, as predicted by (12) and confirmed by the measurement results in Fig. 31(b), simultaneously increasing R_{IN} and reducing C_{IN} enhances the LG at the passband edges. Moreover, Fig. 31(b) further demonstrates that increasing R_{IN} and reducing C_{IN} has a negligible impact on the RX filtering shape and order.

Fig. 32(a) illustrates the measured RX linearity in the presence of in-band and close-in blockers. Two tones, $f_1 = f_{\mathrm{LO}} + f_{3\,\mathrm{dB}}$ and $f_2 = f_{\mathrm{LO}} + \Delta f$, are applied to the RX such that their intermodulation product falls within the desired band. Then, Δf is swept across the close-in blocker range. As shown in Fig. 32(a), simultaneously increasing R_{IN} and reducing C_{IN} improves the IIP3 by approximately 3.8 dB. However, a tradeoff between in-band and out-of-band linearity can be observed. As Δf increases, the IIP3 improvement diminishes due to the lower C_{IN} value. For the IIP3 measurements, two tones at $f_1 = f_{\mathrm{LO}} + \Delta f$ and $f_2 = f_{\mathrm{LO}} + 2\Delta f - 5$ MHz are applied to the RX input, where Δf is the offset frequency from the LO frequency. Δf is then swept to measure the RX IIP3 versus the offset frequency, as shown in Fig. 32(b). The measured in-band IIP3 is -3.4 dBm and reaches 10.4 dBm at $\Delta f / f_{3\,\mathrm{dB}} = 2$.

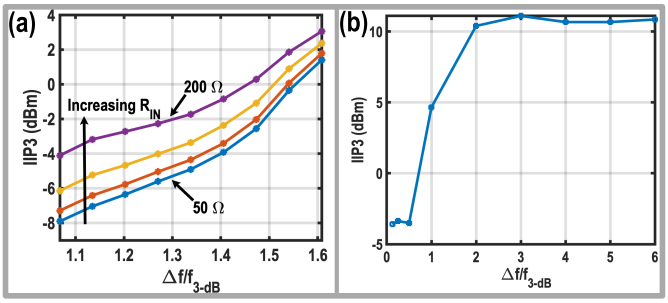

Fig. 32. (a) Reduction of IM3 generated by in-band and close-in blockers through increasing R_{IN} and reducing C_{IN}. (b) Measured IIP3 versus the offset frequency.

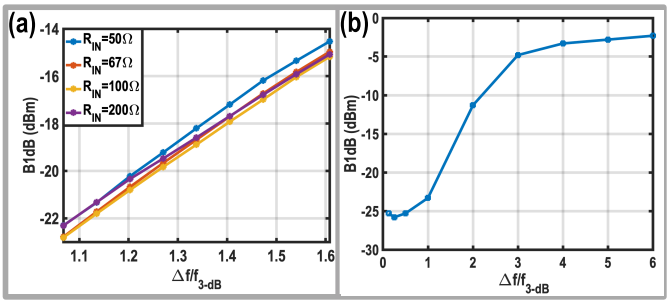

Fig. 33. (a) Effect of increasing R_{IN} and reducing C_{IN} on the measured B1dB across the close-in blocker range. (b) Measured B1dB versus the offset frequency.

To investigate the effect of increasing R_{IN} and reducing C_{IN} on the blocker 1-dB compression point (B1dB) performance, a desired signal at $f_{\mathrm{sig}} = f_{\mathrm{LO}} + 5$ MHz and a blocker at $f_{\mathrm{blk}} = f_{\mathrm{LO}} + \Delta f$ are applied to the RX input. Then, Δf is swept across the close-in blocker range. As illustrated in Fig. 33(a), unlike IIP3, the B1dB of the proposed RX does not improve with increased R_{IN} and reduced C_{IN} across the close-in blocker range, as the large-signal operation of the RX is constrained by the supply voltage. Moreover, Fig. 33(a) shows the measured B1dB versus the blocker offset frequency. The in-band B1dB is -25.8 dBm and increases to -2.3 dBm at far-out offset frequencies.

In the second-order input intercept point (IIP2) measurement shown in Fig. 34(a), two tones are applied at frequencies $f_1 = f_{\mathrm{LO}} + \Delta f$ and $f_2 = f_{\mathrm{LO}} + \Delta f - 5$ MHz, while Δf is swept. The measured in-band IIP2 is 28.6 dBm and increases to 55.4 dBm at $\Delta f / f_{3\,\mathrm{dB}} = 2$. As discussed in Appendix B, to meet the performance requirements for 5G frequency-division duplex (FDD) applications, the proposed

TABLE III
PERFORMANCE SUMMARY AND COMPARISON WITH PRIOR ART

	Lien JSSC 2018 [50]	Bhat JSSC 2022 [36]	Montazerolghaem ISSCC 2021 [27]	Razavi JSSC 2022[30]	This Work
Architecture	Mixer first	Mixer first	LNTA based	LNTA based	LNTA based
Technology	45 nm SOI	22 nm SOI	40 nm	28 nm	40 nm
f_{RF} (GHz)	0.2 - 8	1 - 6	0.4 - 3.2	0.4 - 6	0.4 – 7.3
Gain (dB)	21	22.4	36	54	38
Flat BW	Yes	No	Yes	No	Yes
Single Ended Input	No	No	Yes	Yes	Yes
BW (MHz)	20	350	160	0.2 - 160	300
NF (dB)	2.3 - 7	2.5 - 5	2.7 – 3.6	2.1†/4.42§	3.2 - 5.8
0dBm Blocker NF (dB)	4.7	N/A	8.4	5.2†/7.4§	9.65
Filtering roll-off (dB/dec)	-40	-20	-55	-60	-60
IB OIP3 (dBm)	21	28.5-34.4	17	19$	27-38
OOB IIP_3 (dBm)	39 $\Delta f/\omega_{3\text{-dB}} = 8$	18 $\Delta f/\omega_{3\text{-dB}} = 5.7$	10 $\Delta f/\omega_{3\text{-dB}} = 3$	3$ $\Delta f/\omega_{3\text{-dB}} = 12.5$	11 $\Delta f/\omega_{3\text{-dB}} = 3$
OOB IIP_2 (dBm)	88 $\Delta f/\omega_{3\text{-dB}} = 8$	N/A	50 $\Delta f/\omega_{3\text{-dB}} = 3$	20$ $\Delta f/\omega_{3\text{-dB}} = 12.5$	67.7 $\Delta f/\omega_{3\text{-dB}} = 3$
B1dB(dBm)	12 $\Delta f/\omega_{3\text{-dB}} = 4$	3 $\Delta f/\omega_{3\text{-dB}} = 5.7$	-5 $\Delta f/\omega_{3\text{-dB}} = 5$	N/A	-4.8 $\Delta f/\omega_{3\text{-dB}} = 3$
EVM (dB)	N/A	N/A	-26.4¥	-25.3¢	-31œ
Supply (V)	1.2	0.83	1.3/1.2	1	1.3
Active Area (mm^2)	0.8	0.48	0.6	1.9	0.42
Power (mW)	50mW+ 30mW/GHz	172	58.5+ 17.6mW/GHz	23 - 49	100+ 13mW/GHz

†Low noise mode, § Harmonic reject mode, $ Maximum bandwidth, ¢ -57dBm 80MS/s 64-QAM, , ¥ -60dBm 140MS/s 64-QAM, œ -55dBm 100MS/s 64-QAM.

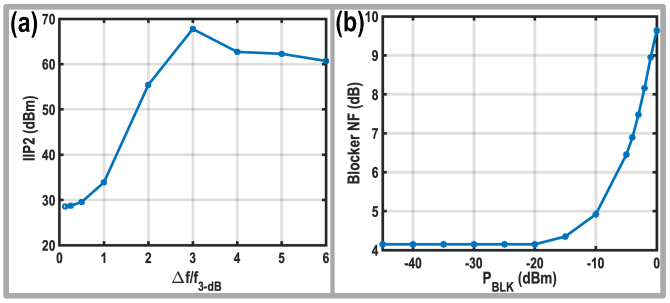

Fig. 34. (a) Measured IIP2 versus the offset frequency. (b) Measured blocker NF versus the blocker power.

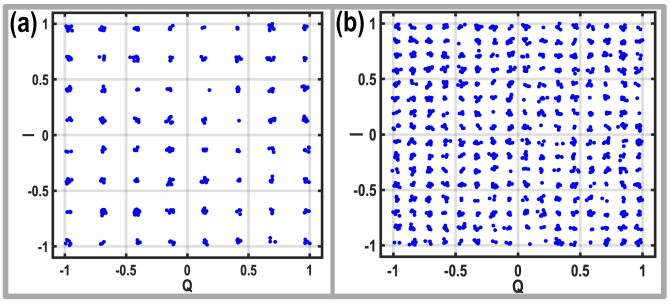

Fig. 35. Measured constellation of the proposed RX for −55-dBm 100-MS/s (a) 64-QAM and (b) 256-QAM input signals.

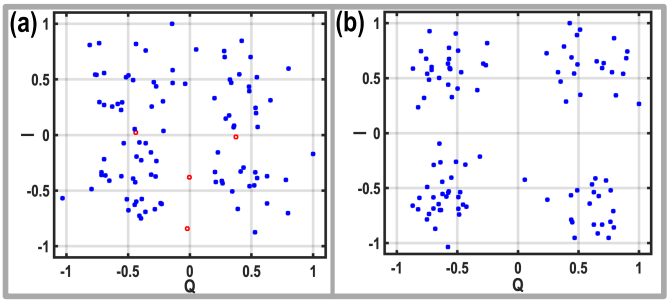

Fig. 36. (a) Measured constellation at the reference sensitivity. (b) Measured constellation in the presence of a −35-dBm in-band blocker.

RX requires a duplexer with isolation greater than 58 dB between its transmitter (TX) and RX ports—an ambitious goal to achieve. Therefore, the IIP2 performance of the proposed RX should be enhanced in future implementations, either by adopting a fully differential LNTA and TIA or by employing calibration techniques similar to those discussed in [18]. The RX NF is also measured in the presence of a blocker located at $\Delta f/f_{3\,\mathrm{dB}} = 5$. As depicted in Fig. 34(b), a 0-dBm blocker degrades the RX NF by 5.5 dB.

Next, the RX performance is evaluated using high-order quadrature amplitude modulation (QAM) schemes, as illustrated in Fig. 35. Applying a −55-dBm 100-MS/s QAM-64 signal to the RX input results in a measured error vector magnitude (EVM) of −31 dB. The EVM slightly degrades to −30.2 dB with a QAM-256 signal while maintaining the same sampling rate and input power.

Following the 3GPP standard, the RX is further evaluated. The first test measures reference sensitivity, where the throughput must exceed 95% for a 50-MS/s QPSK signal with an input power of −87.7 dBm. To measure reference sensitivity, we apply 100 symbols to the input of our RX. As shown in Fig. 36(a), the RX achieves a throughput of 96% for the reference sensitivity, satisfying the 3GPP requirement (96 symbols out of 100 symbols are received correctly). Note that the red dots represent the missing symbols. For blocking tests, the throughput must exceed 95% when the input signal power is 6 dB higher than the reference sensitivity level.

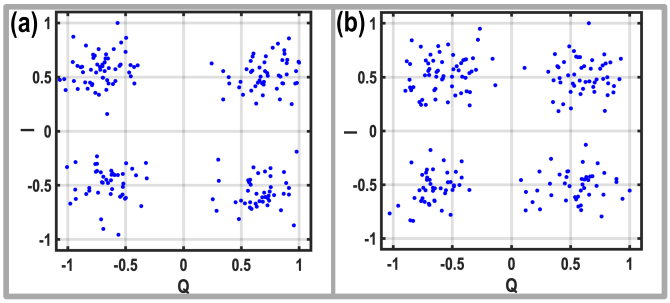

Fig. 37. Measured constellation in the presence of (a) −15-dBm close-in blocker and (b) −4-dBm far-out blocker.

In the in-band blocking test, a −35-dBm 20-MS/s modulated in-band blocker at the passband edge is combined with the desired signal and applied to the RX input. Thanks to the RX's excellent in-band linearity, 100% of the symbols are received correctly, as shown in Fig. 36(b). In the 5G close-in blocking scenario, a −15-dBm close-in blocker at 60 MHz offset frequency from the bandwidth edge is applied to the RX. As illustrated in Fig. 37(a), all the symbols are received correctly, demonstrating the RX's high selectivity. For the co-location blocking test, while receiving the desired signal at 3 GHz, a −4-dBm far-out blocker located at 900 MHz is applied to the RX. The proposed RX receives all the symbols correctly in this scenario as well [Fig. 37(b)]. The measured EVM is −9.9 dB for the far-out blocking test, corresponding to a 1.4-dB signal-to-noise ratio (SNR) degradation caused by reciprocal mixing and the nonlinearity of the proposed RX.

The performance of the proposed RX is summarized in Table III and compared with the state-of-the-art RXs [27], [30], [36], [50] having similar bandwidth and operating frequency. This work demonstrates superior in-band linearity and selectivity. It is also the only RX that has been tested for reference sensitivity and various blocking scenarios specific to local area base station applications, successfully passing all tests.

VII. Conclusion

This article presented a wideband LNTA-based receiver for 5G local area base station applications, covering both the low- and mid-band frequencies. To identify the optimal TIA architecture, the first-order and Rauch TIAs are extensively analyzed and compared in terms of the transfer function, input impedance, LG, and noise. Based on the analysis, the Rauch TIA was chosen for its superior selectivity and higher LG. A third-order high-pass filter was also added in parallel with its feedback resistor to further enhance the selectivity of the Rauch TIA. The RX integrates the Rauch TIAs with passive mixers and an LNTA featuring an N-path notch filter in its feedback. To extend the RX operating frequency, two switch sets at the LNTA output—one for the N-path notch filter and another for the down-converting mixers—were merged. Moreover, the bandpass characteristic of the TIA input impedance is used to introduce positive feedback in the LNTA, enhancing the 3-dB bandwidth without sacrificing the RX's out-of-band rejection. Fabricated in 40-nm bulk CMOS technology, the proposed RX meets the 3GPP requirements for reference sensitivity, in-band blocking, close-in blocking, and out-of-band blocking, making it well suited for 5G local area base station applications.

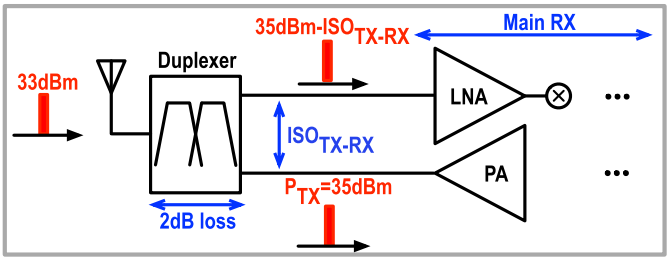

Fig. 38. Front-end block diagram of an FDD transceiver.

Appendix A

According to the 3GPP standard, the RX throughput must exceed 95% when the input signal is a 50-MS/s QPSK signal with a power of −81.7 dBm and a −35-dBm 20 MS/s modulated in-band blocker is present at the passband edge [1]. To calculate the required in-band third-order intercept point (IIP3), the in-band blocker is modeled with two −38-dBm tones ($P_{\text{in},B}$), and the power of the third-order intermodulation tones P_{IM3} is considered 10 dB below the desired signal power to ensure 95% throughput with sufficient margin. The required IIP3 can be derived as follows:

$$\text{IIP3} \geq 1.5\ P_{\text{in},B} - 0.5\ P_{\text{IM3}} \rightarrow \text{IIP3} \geq -11.15\ \text{dBm}. \quad (33)$$

Next, we estimate the minimum RX gain ($G_{\text{RX,min}}$) required to ensure that the quantization noise of the ADC is 10 dB below the IM3 tones at the ADC input, preventing it from limiting the RX throughput. Therefore,

$$P_{\text{IM3}} + G_{\text{RX,min}} - 10\ \text{dB} \geq \text{FS} - 6n - 1.76 \quad (34)$$

where FS is the full-scale input power of the ADC and n is the number of bits. Assuming the use of a 12-bit ADC with FS = +6 dBm as in [37], $G_{\text{RX,min}} \geq 33.7$ dB is required. Thus, the required in-band OIP3 can be estimated as

$$\text{OIP3} = \text{IIP3} + G_{\text{RX,min}} \rightarrow \text{OIP3} \geq 22.55\ \text{dBm}. \quad (35)$$

Appendix B

In FDD systems, as shown in Fig. 38, TX power (P_{TX}) leaks into the RX input due to the limited isolation between the transmitter and receiver ports of the duplexer (denoted as $\text{ISO}_{\text{TX-RX}}$). This leakage generates IM2 in the RX path due to the limited IIP2 of the proposed RX. To prevent degradation of the SNR, the IM2 power (P_{IM2}) caused by the TX leakage must be at least 10 dB lower than the RX reference sensitivity (P_{ref}). Consequently, the required duplexer isolation for a given RX IIP2 performance can be calculated using the following equation:

$$\text{ISO}_{\text{TX-RX}} = (P_{\text{TX}} - 3) - \frac{\text{IIP2} + P_{\text{IM2}}}{2}$$
$$\rightarrow \text{ISO}_{\text{TX-RX}} = (P_{\text{TX}} - 3) - \frac{\text{IIP2} + P_{\text{ref}} - 10}{2} \quad (36)$$

where the −3-dB term accounts for the modulated TX signal. This equation clearly shows the tradeoff between the RX IIP2

and the duplexer ISO_{TX-RX} requirements. According to 3GPP standards for local area base station applications, the reference sensitivity should be better than -87.7 dBm for channel bandwidths greater than 50 MHz, with the transmitter's radiated power at the antenna being 33 dBm. Taking into account a 2-dB loss in the duplexer between the TX and antenna ports, P_{TX} must be approximately 35 dBm. Additionally, considering an RX RF bandwidth of 75 MHz and a frequency spacing of 20 MHz between the RX and TX bandwidth edges, we obtain a ratio of $\Delta f/f_{3-dB} = 1.53$. The measured IIP2 of the proposed RX at this offset frequency is $+46$ dBm. Therefore, to meet the FDD transceiver performance requirements, the proposed RX requires a duplexer with $ISO_{TX-RX} \geq 58$ dB.

ACKNOWLEDGMENT

The authors acknowledge imec, Leuven, Belgium, for handling the tape-out. They also thank Atef Akhnoukh, Zu-Yao Chang, and Dr. Juan Bueno Lopez for their valuable support during the design, fabrication, and measurement phases, and Zhong Gao, Masoud Pashaeifar, and Sajad Golabi for the technical discussions.

REFERENCES

[1] *Base Station (BS) Radio Transmission and Reception (Release 17)*, document TS 38.104, 3GPP, Jun. 2022.

[2] C. Andrews and A. C. Molnar, "A passive mixer-first receiver with digitally controlled and widely tunable RF interface," *IEEE J. Solid-State Circuits*, vol. 45, no. 12, pp. 2696–2708, Dec. 2010.

[3] C. Andrews, L. Diamente, D. Yang, B. Johnson, and A. Molnar, "A wideband receiver with resonant multi-phase LO and current reuse harmonic rejection baseband," *IEEE J. Solid-State Circuits*, vol. 48, no. 5, pp. 1188–1198, May 2013.

[4] A. Nejdel, M. Abdulaziz, M. Törmänen, and H. Sjöland, "A positive feedback passive mixer-first receiver front-end," in *Proc. IEEE Radio Freq. Integr. Circuits Symp. (RFIC)*, May 2015, pp. 79–82.

[5] H. Westerveld, E. Klumperink, and B. Nauta, "A cross-coupled switch-RC mixer-first technique achieving +41 dBm out-of-band IIP3," in *Proc. IEEE Radio Freq. Integr. Circuits Symp. (RFIC)*, May 2016, pp. 246–249.

[6] Y.-C. Lien, E. A. M. Klumperink, B. Tenbroek, J. Strange, and B. Nauta, "High-linearity bottom-plate mixing technique with switch sharing for N -path filters/mixers," *IEEE J. Solid-State Circuits*, vol. 54, no. 2, pp. 323–335, Feb. 2019.

[7] S. Krishnamurthy and A. M. Niknejad, "Design and analysis of enhanced mixer-first receivers achieving 40-dB/decade RF selectivity," *IEEE J. Solid-State Circuits*, vol. 55, no. 5, pp. 1165–1176, May 2020.

[8] V. K. Purushothaman, E. A. M. Klumperink, B. T. Clavera, and B. Nauta, "A fully passive RF front end with 13-dB gain exploiting implicit capacitive stacking in a bottom-plate N-path filter/mixer," *IEEE J. Solid-State Circuits*, vol. 55, no. 5, pp. 1139–1150, May 2020.

[9] G. Pini, D. Manstretta, and R. Castello, "Analysis and design of a 260-MHz RF bandwidth +22-dBm OOB-IIP3 mixer-first receiver with third-order current-mode filtering TIA," *IEEE J. Solid-State Circuits*, vol. 55, no. 7, pp. 1819–1829, Jul. 2020.

[10] S. Krishnamurthy and A. M. Niknejad, "Synthesis and design of enhanced N-path filters with 60-dB/decade RF selectivity," *IEEE Solid-State Circuits Lett.*, vol. 3, pp. 522–525, 2020.

[11] E. Zolkov and E. Cohen, "A mixer-first receiver with enhanced matching bandwidth by using baseband reactance-canceling LNA," *IEEE Solid-State Circuits Lett.*, vol. 4, pp. 109–112, 2021.

[12] S. Krishnamurthy and A. M. Niknejad, "An enhanced mixer-first receiver with distortion cancellation, achieving 80-dB/decade RF selectivity and +8-dBm B1dB for adjacent channel blockers," *IEEE Solid-State Circuits Lett.*, vol. 4, pp. 64–67, 2021.

[13] V. K. Purushothaman, E. A. M. Klumperink, R. Plompen, and B. Nauta, "Low-power high-linearity mixer-first receiver using implicit capacitive stacking with 3× voltage gain," *IEEE J. Solid-State Circuits*, vol. 57, no. 1, pp. 245–259, Jan. 2022.

[14] B. Guo, H. Wang, Y. Wang, K. Li, L. Li, and W. Zhou, "A mixer-first receiver frontend with resistive-feedback baseband achieving 200 MHz IF bandwidth in 65 nm CMOS," in *Proc. IEEE Radio Freq. Integr. Circuits Symp. (RFIC)*, Jun. 2022, pp. 31–34.

[15] S. Araei, S. Mohin, and N. Reiskarimian, "An interferer-tolerant harmonic-resilient receiver with > +10dBm 3rd-harmonic blocker P1 dB for 5G NR applications," in *IEEE Int. Solid-State Circuits Conf. (ISSCC) Dig. Tech. Papers*, Feb. 2023, pp. 18–20.

[16] K. Shi, A. A. Abidi, and H. Darabi, "Second-order transimpedance amplifiers in mixer-first receivers: Design for optimum blocker tolerance," *IEEE Trans. Circuits Syst. I, Reg. Papers*, vol. 70, no. 5, pp. 1821–1834, May 2023.

[17] S. Araei, S. Mohin, and N. Reiskarimian, "Harmonic-resilient fully passive mixer-first receiver for software-defined radios," *IEEE J. Solid-State Circuits*, vol. 58, no. 12, pp. 3396–3407, Dec. 2023.

[18] J. Borremans et al., "A 40 nm CMOS 0.4–6 GHz receiver resilient to out-of-band blockers," *IEEE J. Solid-State Circuits*, vol. 46, no. 7, pp. 1659–1671, Jul. 2011.

[19] F. Lin, P.-I. Mak, and R. P. Martins, "An RF-to-BB-current-reuse wideband receiver with parallel N-path active/passive mixers and a single-MOS pole-zero LPF," *IEEE J. Solid-State Circuits*, vol. 49, no. 11, pp. 2547–2559, Nov. 2014.

[20] J. W. Park and B. Razavi, "Channel selection at RF using Miller bandpass filters," *IEEE J. Solid-State Circuits*, vol. 49, no. 12, pp. 3063–3078, Dec. 2014.

[21] Z. Lin, P.-I. Mak, and R. P. Martins, "Analysis and modeling of a gain-boosted N-path switched-capacitor bandpass filter," *IEEE Trans. Circuits Syst. I, Reg. Papers*, vol. 61, no. 9, pp. 2560–2568, Sep. 2014.

[22] C.-K. Luo, P. S. Gudem, and J. F. Buckwalter, "A 0.4–6-GHz 17-dBm B1dB 36-dBm IIP3 channel-selecting low-noise amplifier for SAW-less 3G/4G FDD diversity receivers," *IEEE Trans. Microw. Theory Techn.*, vol. 64, no. 4, pp. 1110–1121, Apr. 2016.

[23] L. Zhang, A. Natarajan, and H. Krishnaswamy, "Scalable spatial notch suppression in spatio-spectral-filtering MIMO receiver arrays for digital beamforming," *IEEE J. Solid-State Circuits*, vol. 51, no. 12, pp. 3152–3166, Dec. 2016.

[24] G. Qi, P.-I. Mak, and R. P. Martins, "A 0.038-mm^2 SAW-less multiband transceiver using an N-path SC gain loop," *IEEE J. Solid-State Circuits*, vol. 52, no. 8, pp. 2055–2070, Aug. 2017.

[25] G. Qi, B. van Liempd, P. Mak, R. P. Martins, and J. Craninckx, "A SAW-less tunable RF front end for FDD and IBFD combining an electrical-balance Duplexer and a switched-LC N-path LNA," *IEEE J. Solid-State Circuits*, vol. 53, no. 5, pp. 1431–1442, May 2018.

[26] H. Wang, Z. Wang, and P. Heydari, "A wideband blocker-tolerant receiver with high-Q RF-input selectivity and <-80dBm LO leakage," in *IEEE Int. Solid-State Circuits Conf. (ISSCC) Dig. Tech. Papers*, Feb. 2019, pp. 450–452.

[27] M. A. Montazerolghaem, S. Pires, L. C. N. de Vreede, and M. Babaie, "A 3dB-NF 160MHz-RF-BW blocker-tolerant receiver with third-order filtering for 5G NR applications," in *IEEE Int. Solid-State Circuits Conf. (ISSCC) Dig. Tech. Papers*, vol. 64, Feb. 2021, pp. 98–100.

[28] H. Wang, Z. Wang, and P. Heydari, "An LO leakage suppression technique for blocker-tolerant wideband receivers with high-Q selectivity at RF input," *IEEE J. Solid-State Circuits*, vol. 56, no. 6, pp. 1682–1696, Jun. 2021.

[29] M. A. Montazerolghaem, L. C. N. de Vreede, and M. Babaie, "A 0.5–3 GHz receiver with a parallel preselect filter achieving 120dB/dec channel selectivity and +28 dBm out-of-band IIP3," in *Proc. IEEE Custom Integr. Circuits Conf. (CICC)*, Apr. 2022, pp. 11–12.

[30] H. Razavi and B. Razavi, "A 0.4–6 GHz receiver for cellular and WiFi applications," *IEEE J. Solid-State Circuits*, vol. 57, no. 9, pp. 2640–2657, Sep. 2022.

[31] M. A. Montazerolghaem, L. C. N. de Vreede, and M. Babaie, "A highly linear receiver using parallel preselect filter for 5G microcell base station applications," *IEEE J. Solid-State Circuits*, vol. 58, no. 8, pp. 2157–2172, Aug. 2023.

[32] B. Guo, H. Wang, L. Li, and W. Zhou, "A 65 nm CMOS current-mode receiver frontend with frequency-translational noise cancelation and 425 MHz IF bandwidth," in *Proc. IEEE Radio Freq. Integr. Circuits Symp. (RFIC)*, Jun. 2023, pp. 21–24.

[33] M. A. Montazerolghaem, L. C. N. de Vreede, and M. Babaie, "A highly selective receiver with programmable zeros and second-order TIA," *IEEE J. Solid-State Circuits*, vol. 59, no. 6, pp. 1668–1683, Jun. 2024.

[34] I. Fabiano, M. Sosio, A. Liscidini, and R. Castello, "SAW-less analog front-end receivers for TDD and FDD," *IEEE J. Solid-State Circuits*, vol. 48, no. 12, pp. 3067–3079, Dec. 2013.

[35] D. H. Mahrof, E. A. M. Klumperink, Z. Ru, M. S. O. Alink, and B. Nauta, "Cancellation of OpAmp virtual ground imperfections by a negative conductance applied to improve RF receiver linearity," *IEEE J. Solid-State Circuits*, vol. 49, no. 5, pp. 1112–1124, May 2014.

[36] A. N. Bhat, R. A. R. van der Zee, and B. Nauta, "A baseband-matching-resistor noise-canceling receiver with a three-stage inverter-only OpAmp for high in-band IIP3 and wide IF applications," *IEEE J. Solid-State Circuits*, vol. 56, no. 7, pp. 1994–2006, Jul. 2021.

[37] D. J. McLaurin et al., "A highly reconfigurable 65 nm CMOS RF-to-bits transceiver for full-band multicarrier TDD/FDD 2G/3G/4G/5G macro basestations," in *IEEE Int. Solid-State Circuits Conf. (ISSCC) Dig. Tech. Papers*, Feb. 2018, pp. 162–164.

[38] M. A. Montazerolghaem, L. C. N. de Vreede, and M. Babaie, "A 300 MHz-BW, 27-to-38dBm in-band OIP3 sub-7 GHz receiver for 5G local area base station applications," in *IEEE Int. Solid-State Circuits Conf. (ISSCC) Dig. Tech. Papers*, Feb. 2023, pp. 292–294.

[39] H. Jung, D. R. Utomo, S.-K. Han, J. Kim, and S.-G. Lee, "An 80 MHz bandwidth and 26.8 dBm OOB IIP3 transimpedance amplifier with improved nested feedforward compensation and multi-order filtering," *IEEE Trans. Circuits Syst. I, Reg. Papers*, vol. 67, no. 10, pp. 3410–3421, Oct. 2020.

[40] B. Razavi, "The transimpedance amplifier [a circuit for all seasons]," *IEEE Solid State Circuits Mag.*, vol. 11, no. 1, pp. 10–97, Winter. 2019.

[41] D. Murphy et al., "A blocker-tolerant, noise-cancelling receiver suitable for wideband wireless applications," *IEEE J. Solid-State Circuits*, vol. 47, no. 12, pp. 2943–2963, Dec. 2012.

[42] H. Hedayati, W. A. Lau, N. Kim, V. Aparin, and K. Entesari, "A 1.8 dB NF blocker-filtering noise-canceling wideband receiver with shared TIA in 40 nm CMOS," *IEEE J. Solid-State Circuits*, vol. 50, no. 5, pp. 1148–1164, May 2015.

[43] M. K. Lenka and G. Banerjee, "A wideband blocker-tolerant receiver with frequency-translational resistive feedback," *IEEE Trans. Very Large Scale Integr. (VLSI) Syst.*, vol. 27, no. 5, pp. 993–1006, May 2019.

[44] P. Wambacq and W. M. Sansen, *Distortion Analysis of Analog Integrated Circuits*, vol. 451. Cham, Switzerland: Springer, 2013.

[45] X. Li, F. Yin, and J. C. Rudell, "Effects of receiver input impedance on nonlinear distortion in full-duplex radios," in *Proc. IEEE Int. Symp. Circuits Syst. (ISCAS)*, May 2021, pp. 1–5.

[46] B. Razavi, *RF Microelectronics*, vol. 2. New York, NY, USA: Prentice-Hall, 2012.

[47] H. Zhang and E. Sánchez-Sinencio, "Linearization techniques for CMOS low noise amplifiers: A tutorial," *IEEE Trans. Circuits Syst. I, Reg. Papers*, vol. 58, no. 1, pp. 22–36, Jan. 2011.

[48] X. He and H. Kundur, "A compact SAW-less multiband WCDMA/GPS receiver front-end with translational loop for input matching," in *IEEE Int. Solid-State Circuits Conf. (ISSCC) Dig. Tech. Papers*, Apr. 2011, pp. 372–374.

[49] B. Nauta, "A CMOS transconductance-C filter technique for very high frequencies," *IEEE J. Solid-State Circuits*, vol. 27, no. 2, pp. 142–153, Feb. 1992.

[50] Y.-C. Lien, E. A. M. Klumperink, B. Tenbroek, J. Strange, and B. Nauta, "Enhanced-selectivity high-linearity low-noise mixer-first receiver with complex pole pair due to capacitive positive feedback," *IEEE J. Solid-State Circuits*, vol. 53, no. 5, pp. 1348–1360, May 2018.

Mohammad Ali Montazerolghaem (Member, IEEE) received the B.Sc. degree in electrical engineering from the University of Isfahan, Isfahan, Iran, in 2012, and the M.Sc. degree from the Amirkabir University of Technology, Tehran, Iran, in 2014. He is currently pursuing the Ph.D. degree with the ELCA Research Group, Delft University of Technology, Delft, The Netherlands.

In December 2022, he joined Renesas Electronics, 's-Hertogenbosch, The Netherlands, where he is currently a Senior RFIC Designer. His research interests include high-performance receivers for 5G cellular, base station applications, and low-power transceivers for IoT applications.

Mr. Montazerolghaem serves as a reviewer for IEEE JOURNAL OF SOLID-STATE CIRCUITS, IEEE SOLID-STATE CIRCUITS LETTERS, and IEEE TRANSACTIONS ON CIRCUITS AND SYSTEMS—I: REGULAR PAPERS.

Masoud Babaie (Senior Member, IEEE) received the B.Sc. degree (Hons.) in electrical engineering from the Amirkabir University of Technology, Tehran, Iran, in 2004, the M.Sc. degree in electrical engineering from the Sharif University of Technology, Tehran, in 2006, and the Ph.D. degree (cum laude) in electrical engineering from Delft University of Technology, Delft, The Netherlands, in 2016.

From 2006 to 2011, he was with the Kavoshcom Research and Development Group, Tehran, focusing on wireless communication system design. He was a Visiting Scholar with Berkeley Wireless Research Center, Berkeley, CA, USA, from 2014 to 2015. In 2016, he joined Delft University of Technology, where he is currently an Associate Professor. He has authored or co-authored one book, three book chapters, 11 patents, and over 100 peer-reviewed technical papers. His research interests include RF and millimeter-wave integrated circuits, systems for wireless communications, and cryogenic electronics for quantum computing.

Dr. Babaie has received several accolades, including the 2015–2016 IEEE Solid-State Circuits Society Pre-Doctoral Achievement Award, the 2019 IEEE ISSCC Demonstration Session Certificate of Recognition, the 2020 IEEE ISSCC Jan Van Vessem Award for Outstanding European Paper, the 2022 IEEE CICC Best Paper Award, the 2023 IEEE IMS Best Student Paper Award (second place), the 2024 IEEE Solid-State Circuits Society Outstanding Reviewer, and the 2025 IEEE Solid-State Circuits Society New Frontier Award. In 2019, he was awarded the Veni Grant from The Netherlands Organization for Scientific Research (NWO). Since 2021, he served on the Technical Program Committee for the IEEE International Solid-State Circuits Conference (ISSCC), where he serves as the RF Subcommittee Interim Vice-Chair for the term of 2025–2026. He has been the Co-Chair of the Emerging Computing Devices and Circuits Subcommittee of the IEEE European Solid-State Electronics Research Conference (ESSERC) since 2022. Additionally, he serves as an Associate Editor for IEEE SOLID-STATE CIRCUITS LETTERS.